POLITECNICO DI TORINO

Collegio di Ingegneria Meccanica, Aerospaziale e dell'Autoveicolo

Corso di Laurea Magistrale in
INGEGNERIA MECCANICA (MECHANICAL ENGINEERING)

Master Thesis

A Comparative Multi-Method Study of Uniform and Graded TPMS Lattices Fabricated via Additive Manufacturing.

Supervisor:
Prof. Abdollah Saboori

Co-supervisor:
Dr. Mohammad Taghian

Candidate:
Pouya Azarandaz

July 2025

Abstract:

With emphasis on the Face-Centered Rhombic Dodecahedron (FRD) topology, this thesis examines the mechanical behavior and structural performance of triply periodic minimal surface (TPMS) lattice structures made using Laser Powder Bed Fusion (L-PBF). For comparison, the uniform and functionally graded variations (FRD-30, FRD-40, and FRD-45) were evaluated against Gyroid and Fischer–Koch–S structures. They were developed with a constant average volume percentage of 45%. The relationship between relative density and the mechanical performance of these designed materials was further validated by Ashby-Gibson modeling.

The evaluation of internal porosity, defect morphology, and geometric integrity was done using high-resolution X-ray computed tomography (XCT). According to the results, the Fischer-Koch-S structure had the most uniform defect distribution and the lowest pore volume, and generally the printing accuracy was acceptable.

In comparison to the uniform FRD-45, Gyroid, and Fischer-Koch-S, FRD - 30 showed better deformation control and smoother stress-strain responses, according to mechanical tests conducted under quasi-static compression in accordance with ISO 13314 standards. Particularly, among the structures examined, FRD-40 had the highest elastic modulus, indicating higher stiffness and load-bearing capacity. The Fischer–Koch–S lattice demonstrated its efficiency for energy-dissipating applications by achieving the highest absorbed and specific energy absorption among all studied configurations.

The predictive accuracy of the numerical models was confirmed by finite element simulations, which replicated the experimentally observed deformation behavior and stress localization. Additionally, the Ashby-Gibson model's application demonstrated how relative density affects mechanical performance, with variations due to design complexity and defects in the process.

To further investigate the failure mechanisms, fracture surfaces of the tested specimens were analyzed using Scanning Electron Microscopy (SEM). The micrographs revealed key fracture features such as delamination zones, the presence of unfused powder particles and porosities inside the structures. These observations highlighted the role of process-induced defects and local structural anisotropy in crack initiation and propagation.

Overall, this work confirms that functional grading and topology optimization significantly enhance the mechanical efficiency of TPMS lattice structures. The integrated experimental, analytical, and numerical approach provides valuable insights for the design of advanced architected materials in aerospace, automotive, and biomedical applications.

Keywords:

TPMS Structures, Additive Manufacturing, Finite Element Analysis, CT Characterization, Microstructural characterization

Acknowledgments

I want to express my sincere gratitude to Dr. Saboori, my excellent supervisor, for his important advice, knowledge, and consistent encouragement along this trip. His advice and support have been invaluable in helping me finish this thesis. I sincerely appreciate his commitment and guidance, which enabled me to accomplish this.

I would like to express my deepest gratitude to my parents and my brother, whose unwavering love, sacrifices, and constant support have been the foundation of all my achievements. Their belief in me, even during the most challenging times, gave me the strength and motivation to persevere. This thesis is not only the culmination of my academic journey but also a reflection of the values, patience, and resilience they have instilled in me throughout my life. I dedicate this work to them with all my heart.

I would also like to extend my sincere thanks to my friends and colleagues, whose companionship, encouragement, and insightful discussions have greatly enriched my academic experience. Whether through shared challenges in the lab, helpful exchanges of ideas, or simply their presence during long working days, their support has been both motivating and invaluable. I am truly grateful for the collaborative spirit and friendship that made this journey more meaningful and enjoyable.

Finally, I would like to express my heartfelt appreciation to the faculty and staff of the Integrated Additive Manufacturing Lab at Politecnico di Torino. Their expertise, guidance, and the collaborative research environment they foster have played a vital role in the successful completion of this work. The access to advanced resources, technical support, and the spirit of innovation within the lab provided an ideal setting for the development of this thesis. I am truly grateful for their continuous support and commitment to academic excellence.

Table of Contents

Figures

Tables

Table of Abbreviations

Abbreviations	Definition
AM	Additive Manufacturing
ASTM	American Society for Testing and Materials
CAD	Computer-Aided Design
CMP	Coarse Melt Pool
CT	Computed Tomography
CTE	Coefficient of Thermal Expansion
DED	Directed Energy Deposition
DLP	Digital Light Processing
EB-PBF	Electron Beam Powder Bed Fusion
EBSD	Electron Backscatter Diffraction
EDS	Energy-Dispersive X-ray Spectroscopy
EDAX	Energy Dispersive X-ray Analysis
EPC	Eplus Control Software
FE	Finite Element
FMP	Fine Melt Pool
FRD	Face-Centered Rhombic Dodecahedron
GLS	Graded Lattice Structure
HAZ	Heat Affected Zone
ISO	International Organization for Standardization
IPF	Inverse Pole Figure
L-PBF	Laser Powder Bed Fusion
SEM	Scanning Electron Microscopy
SLM	Selective Laser Melting
STL	Stereolithography (file format)
TPMS	Triply Periodic Minimal Surface
UCS	Ultimate Compressive Strength
ULS	Uniform Lattice Structure
VED	Volumetric Energy Density
VF	Volume Fraction
W-EDM	Wire Electrical Discharge Machining
XCT	X-ray Computed Tomography
3D	3-Dimensional

Graphical Abstract:

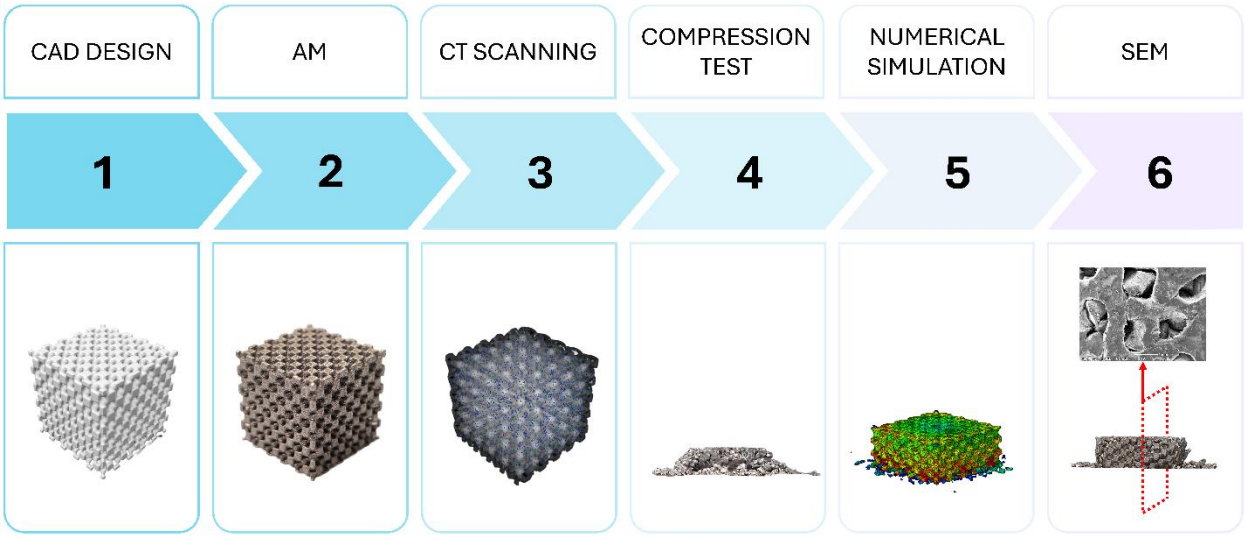

Highlights

- Functionally graded and uniform lattice structures were fabricated via L-PBF.
- CT-scan analysis revealed that structural grading influences internal porosity and defect distribution.
- Quasi-static compression tests followed ISO 13314 standards and confirmed enhanced performance of graded structures.
- Fischer-Koch-S lattice achieved the highest specific energy absorption among the topologies tested.
- Ashby-Gibson model supported the mechanical trends.
- Finite element simulations closely matched experimental results.
- FRD – 40 has experienced the highest stiffness among the tested structures.
- Unfused powder particles, delamination and porosities are the reasons of stress concentration.

1. Introduction

1.1. Additive Manufacturing

In contrast to conventional subtractive manufacturing methods—which shape parts by removing material—additive manufacturing (AM) constructs components in a layer-by-layer manner directly from digital models. This technique offers exceptional geometric freedom, enabling the fabrication of complex parts with high dimensional accuracy and significantly reduced material wastage [1-4]. One of AM's distinct advantages is its ability to create intricate structures without the need for bespoke tooling, since components can be produced directly from raw material using AM systems [5, 6]. Furthermore, AM supports a wide range of material options, making it a versatile platform for manufacturing. Among the most commonly used are thermoplastics [7], photopolymers [8], ceramics [9, 10], metals and their alloys [11], as well as composites and biomaterials[12, 13]. These diverse material capabilities have facilitated the adoption of AM in numerous domains, including biomedical engineering, aerospace, automotive, marine, and even consumer goods [14, 15].

According to ASTM standards, additive manufacturing processes can be broadly categorized into seven principal types: material extrusion, vat photopolymerization, material jetting, sheet lamination, powder bed fusion, direct energy deposition, and binder jetting [16]. In addition to these well-established methods, two emerging techniques, cold spraying and additive friction stir deposition, have also gained recognition for their unique processing routes and potential applications [17]. (Figure 1)

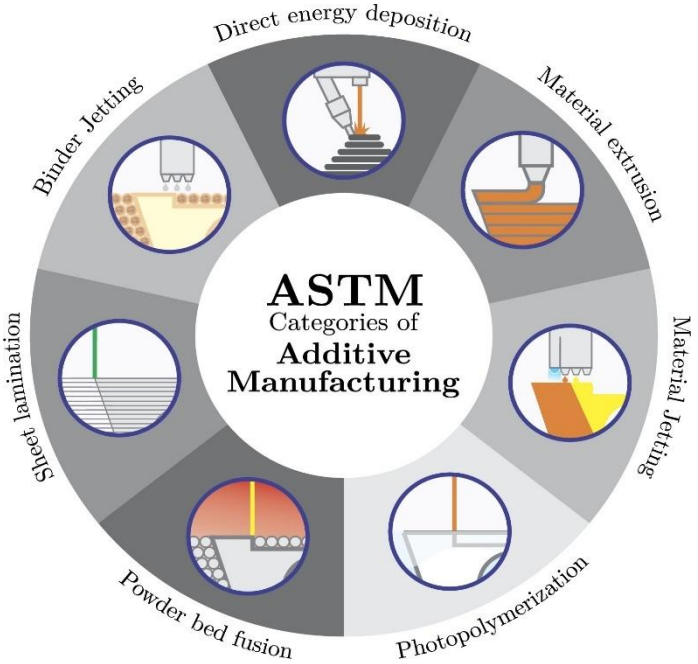

Figure 1. AM categories[18].

1.1.1. Powder Bed Fusion

Powder Bed Fusion (PBF) is widely regarded as a leading additive manufacturing (AM) technique due to its exceptional capability to produce both metallic and non-metallic components with high accuracy. One of its key strengths is the ability to fabricate uniform alloy parts with superior mechanical properties while supporting complex, free-form geometries [19]. Unlike Directed Energy Deposition (DED)—which utilizes a laser, electron beam, or arc as a heat source to melt the material feedstock—PBF operates by sequentially depositing and fusing thin powder layers on top of one another. Despite these advantages, PBF is limited by the dimensions of its build chamber, restricting the fabrication of large-scale parts [20],[21],[22]. For AM to be widely used in industry, produced goods must have the appropriate qualities for the intended use while maintaining competitive manufacturing costs. Therefore, it is essential to carefully examine a variety of chemical and physical phenomena over a range of time and length scales in order to enhance our basic understanding of AM metal processing (Figure 2)[23].

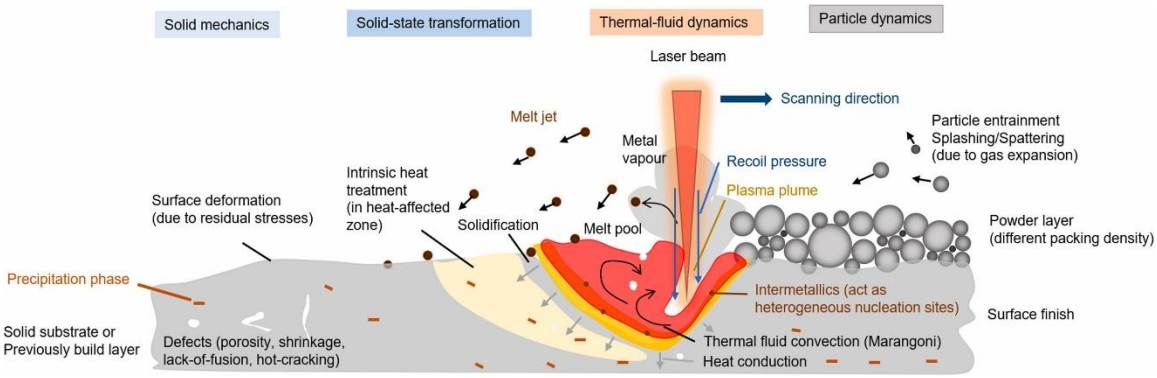

Figure 2. Diagrammatic representation of the Laser-Powder Bed Fusion (L-PBF) process and related physical and chemical processes, demonstrating the many phenomena impacted by solidification, solid-state transformation, and laser-powder interaction [23].

A specific variant of PBF, Laser Powder Bed Fusion (L-PBF), utilizes a laser as its heat source, offering enhanced precision and process control. In L-PBF, solid parts are created through the heating, melting, and solidification of powdered materials. Lasers and electron beams serve as the primary energy sources, enabling high-resolution manufacturing. The process continues as each new layer of powder is spread over the previously fused layer using a recoater blade or roller (see Figure 3).

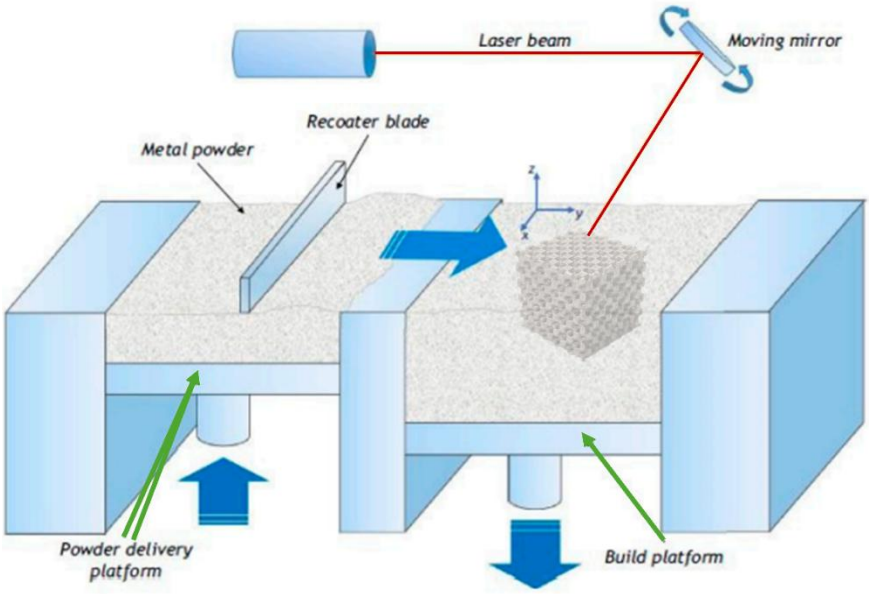

Figure 3. Schematic of the L-PBF Process.

In L-PBF, unmelted powder particles within the bed provide inherent support for the structure being built. After each powder layer is melted and solidified, the build platform lowers to allow the deposition and fusion of the next layer. The process is characterized by high thermal gradients, with heating rates ranging from 10^3 to 10 K/s [24]. L-PBF is particularly effective for fabricating complex geometries across a wide range of materials, though it still necessitates the use of support structures.

L-PBF has proven especially advantageous for producing metals and alloys with gradient structures, enabling the creation of intricate architectural features. However, several challenges persist. These include suboptimal densification under certain process conditions and the tendency of gradient structures to develop significantly larger grain sizes, often exceeding 100 nm. To mitigate these issues, fine-tuning key parameters—such as laser power density, powder feed rate, scan speed, and hatch spacing—on a per-alloy basis is crucial [25].

A major challenge in L-PBF involving metallic powders lies in determining the optimal process window that ensures superior microstructural integrity and mechanical performance. As a result, considerable research has been devoted to parameter optimization, generally categorized into three domains: laser-related parameters, powder characteristics, and powder-bed attributes [26].

1.1.2. Process parameters

Laser power (P), laser scan rate (V), hatching distance, and layer thickness are the primary process parameters in fusion-based additive manufacturing techniques. The process parameters used by the DED and LPBF approaches differ. Because of the simultaneous delivery of feedstock and laser in the DED process, a lower laser scan rate and higher laser power are employed to guarantee that the melt pool is sufficiently large to receive and melt the metallic particles. Instead, higher scan rates, finer powders, and lower laser power are used in the L-PBF process since it requires less energy to produce a fully dense part from already-stationed powders [27]. Furthermore, it has been demonstrated that the DED and L-PBF approaches produce different solidification microstructures due to variations in the melting process and heat transmission modes. From the perspective of in-situ alloying, the L-PBF approach is more susceptible to the feedstock particles' size distribution and shape, both of which have an effect on the mixture's flowability. In fact, the powder layer must be evenly distributed around the building platform in order to attain a homogenous composition; hence, the powder mixture's followability is crucial in this respect. In contrast, the DED approach relies heavily on the carrier gas pressure to regulate the feedstock's flowability. To guarantee a complete and smooth transfer of the powders from the reservoir container to the melt pool, this should be properly implemented.

Pre-alloyed powders are primarily used in L-PBF processes [28-30]. Nevertheless, the L-PBF procedure has been employed in several studies to create the final composition using elemental powder mixes [31-39].Nevertheless, elemental powders are used more frequently in the DED process because, in addition to the advantages of a larger melt pool and higher laser powers, the technique allows for independent adjustment of the powder flow from separate nozzles, which increases control over the chemical composition. The ability to create gradient compositions is another benefit of this feature. While L-PBF processes are known to allow for the creation of finer details, in-situ alloying by L-PBF can occasionally result in parts that suffer from the so-called "unmelted particle-Keyhole" dilemma, in which keyhole formation occurs because the particles are only fully melted at higher energy densities [40], [41].

In the following graph you observe the main process parameters used in AM (Figure 4) and the schematic of L-PBF processing parameters are described in Figure 5.

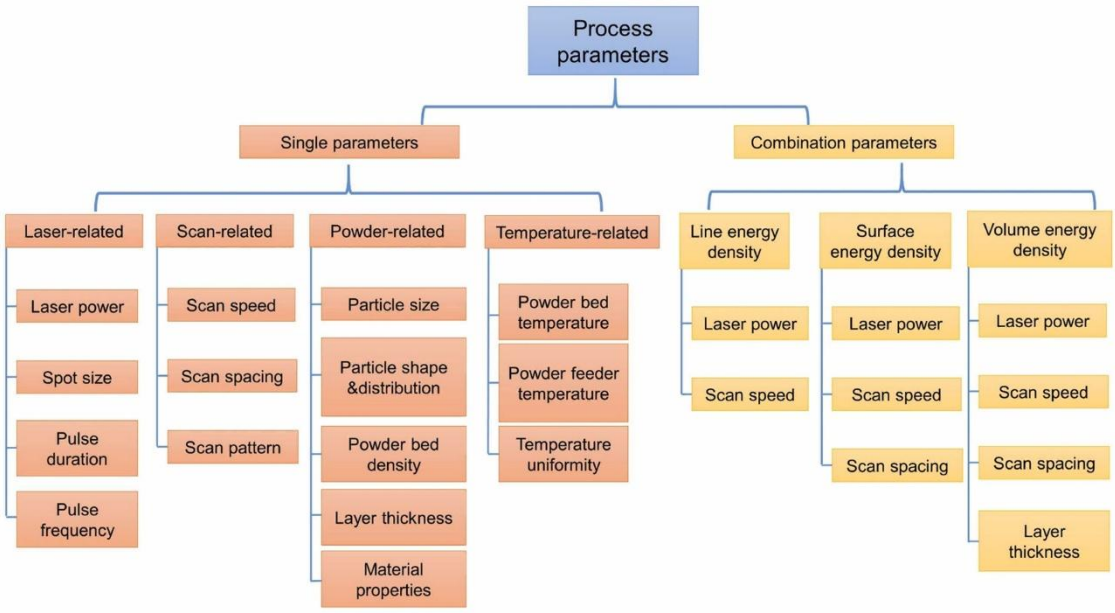

Figure 4. Main process parameters [42].

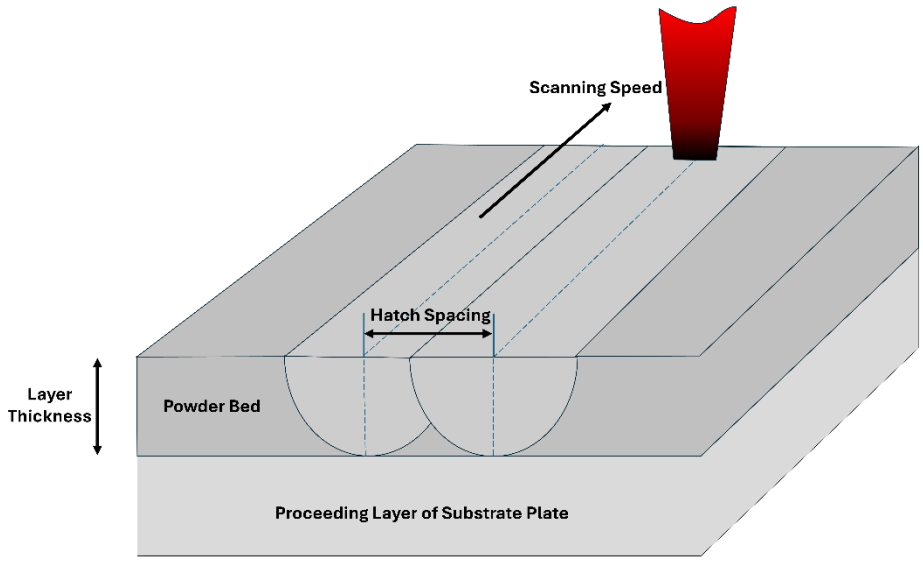

Figure 5. schematic of L-PBF processing parameters.

1.2. Triply Periodic Minimal Surfaces

Triply periodic minimal surface (TPMS) structures, characterized by their zero average curvature surfaces, have become attractive options for advanced material design in a number of fields, such as mechanical engineering, aerospace, and biomedical applications [43](Figure 6). These structures mark an evolution in the field of cellular solids because they combine mechanical strength and geometric simplicity. The mechanical characteristics of conventional cellular

materials including foams, lattice structures, and honeycombs have long been examined; nevertheless, because of their special geometric arrangement, TPMS structures provide clear advantages [44].

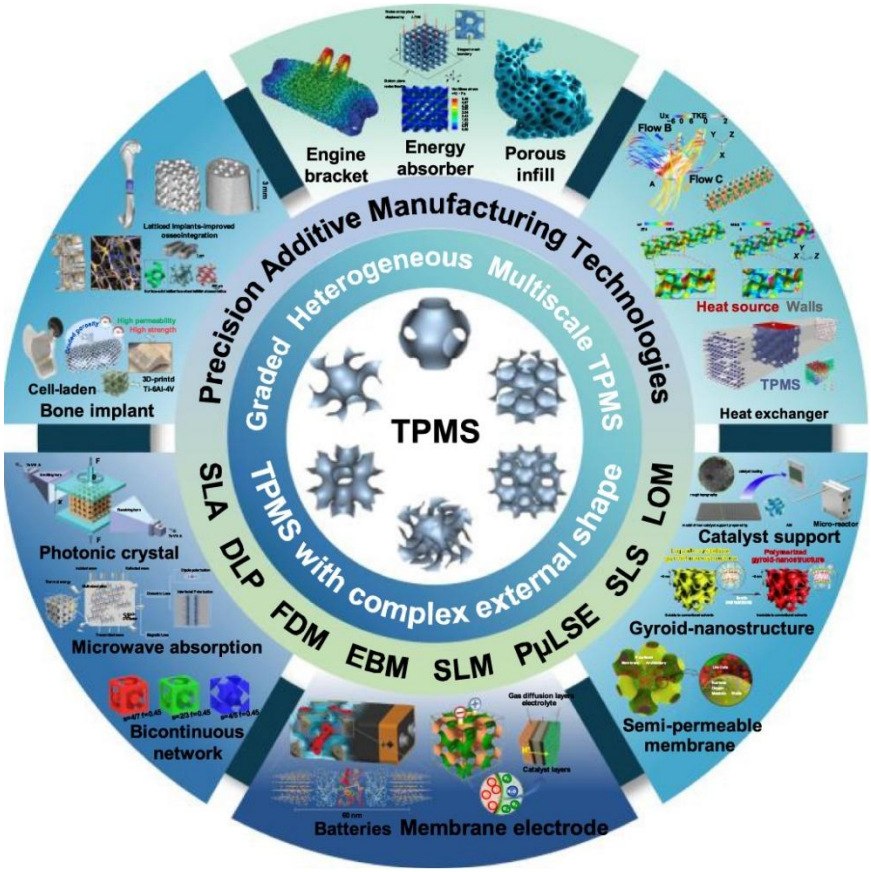

Figure 6. Applications of using TPMS structures [43].

The smooth and continuous surfaces of TPMS structures, which are based on mathematical principles, are a characteristic of minimal surface geometry [45]. The Gyroid, Diamond, and Schwarz'P are TPMS structures that are frequently investigated and have complex mathematical models associated with them [46]. However, because of the intricacy of their geometric features, the production of TPMS structures using conventional techniques frequently fails to guarantee the reliability and accuracy of the final samples [47].

With formerly uncommon control and precision in creating complex geometries like TPMS structures, AM technologies have completely changed the fabrication environment [48, 49]. To create TPMS structures with exceptional mechanical qualities, researchers have used methods including digital light processing (DLP) and L-PBF [50, 51]. The deformation mechanisms and energy absorption capacities of TPMS structures under varied loading conditions have been clarified by experimental investigations and computational simulations [44, 52].

Graded lattice structures (GLSs) are distinguished by their arrangement of multiple materials, diverse cell types, and varying volume fraction (VF) and unit cell size [53-61]. A key advantage of GLSs lies in their capacity to introduce diverse functionalities in specific regions. For example, functionally graded acetabular shells have been designed with high porosity to enhance cell-material interactions and a hard coating and to improve wear resistance [62]. Similarly, helmets are optimized with varying foam densities in different zones to accommodate different levels of damage tolerance and impact probability [63, 64]. Additionally, the graded design of GLSs enables them to exhibit novel properties such as comprehensive mechanical characteristics, high energy absorption capacity, and controllable permeability [54, 65-69]. Until now, prior research on GLSs produced by L-PBF has primarily concentrated on manufacturing processes, static mechanical responses, permeability, and energy absorption capabilities [53, 59, 60, 67, 68, 70, 71].

1.2.1. Mechanical Applications

A thorough analysis of the fundamental mechanical properties of TPMS porous structures has been conducted. TPMS structures can be used as impact absorbers [72] or energy absorbers [73, 74] depending on the long linear elastic stage. TPMS can also be used as vibration isolators because of the mechanical vibration bandgaps [75]. It appears that under the same envelope volume, the weight of TPMS is substantially less than that of the solid structure. TPMS can be utilized as lightweight structures to reduce energy and material usage. Sandwich panels are used extensively in the automotive and aeronautical engineering fields. Two face panels with solid constructions and inner cores made of porous materials make up typical sandwich panels. Lattice cores were used in the design of the majority of sandwich panels throughout the previous few decades. New sandwich panels have recently been built using the TPMS structures as a basis [76]. The suggested techniques can be used to achieve desired bending characteristics and energy absorption capacity. The performance of sandwich panels with honeycomb, lattice, and TPMS cores was compared by Alshaer and Harland [77]. According to experimental data, TPMS cores may achieve the maximum strength, modulus, and stiffness to weight ratio. Furthermore, the TPMS structures are immediately practical as useful elements in the real engineering field. TPMS structures were used as turbine blades by Alkebsi et al. [78]. TPMS's porosity distribution was created using the topology optimization technique. The lightweight, stress, and deformation characteristics were optimized in comparison to the original model. Wang et al. attempted to use TPMS structures to create a soft robot joint [79]. The linear variable stiffness can be obtained by further adjusting the TPMS parameters. It's interesting to note that Pan et al. use TPMS structures to create flexure hinges [80]. The P surface is the best option for flexure hinges, according to experimental results. The compliance and compliance ratio can be significantly increased as compared to conventional leaf flexure hinges. Apart from the examples mentioned above, TPMS structures continue to find several novel uses in the mechanical field.

1.2.2. Biological Applications

TPMS structures have been used extensively in the biological field lately. In fact, TPMS's topology and geometry resemble those of natural systems. As a result, TPMS has many exceptional advantages for biological applications. Typical biological uses for porous TPMS structures include medical implants and scaffolds for tissue engineering. Distinct from the flat surfaces of TPMS, unlike traditional lattice or foam arrangements, allow cells to adhere and grow. Furthermore, there is enough space for the transportation of waste and nutrients thanks to the tightly connected porous structures and high-volume specific surface areas. Because of its superior biological capabilities and the previously described adjustable mechanical mass transfer capabilities, TPMS structures have been successfully used in modern biological engineering.

The structural impacts on cell seeding and culturing were evaluated between TPMS scaffolds and regular saltleached scaffolds in order to confirm the topology advantages of TPMS structures [81]. The porosity of G structures was 10 times greater than that of salt-leached scaffolds thanks to the connected pores. After five days of static culture, as seen in Figure 7(a), sizable cell populations are visible in the middle of the TPMS scaffolds. On the outside of salt-leached scaffolds, however, only cell sheets are visible. Tikhonov et al. created TPMS using calcium phosphates and PEGDA-based hydrogels as a bone defect filler [82], as demonstrated in Figure 7(b). By modifying the TPMS structures' characteristics, the mechanical qualities can be easily changed. The early osteo-integration of Ti6Al4V scaffolds created by TPMS was also covered by Li et al. [83]. The histology findings are displayed in Figure 7(c). TPMS scaffolds can promote the formation of new bone. After five weeks after implantation, a stable contact between the implants and the surrounding bone tissues was achieved. The micro-CT results show clear bone growth surrounding all of the TPMS porosity structures. Hsieh et al. compared the performances of lattice and TPMS scaffolds [84], as shown in Figure 7(d), to show the distinctions with other types of porous structures. Compared to the octet truss lattice, more bone development was seen in the TPMS scaffolds. Furthermore, TPMS scaffolds were less likely than lattice to fail due to fatigue. The recommended TPMS pore diameters for various bone phases were compiled by Barba et al. [85] and are shown in Figure 7(e). For bone colonization or bone vascularization, TPMS can be built with a range of hole diameters because of its variable porosity. In bigger unit cells, Neovius and IWP architectures can provide appropriate osseointegration zones. Alabort et al. used 3D printing to confirm the feasibility of using TPMS as metallic bones [86]. TPMS structures can provide ideal osseo-integration. Figure 7(f) illustrates how TPMS may replicate cortical and trabecular bones with the appropriate stiffness and strength. TPMS constructions have recently been used to support various natural bones. TPMS structures were used as meniscal implants by Zhu et al. [87]. Higher magnitude compression and shear pressures on the articular cartilage can be avoided as compared to commercial solid meniscal implants. The TPMS meniscal implants can preserve certain semilunar features. For cranial bone restoration, Pare et al. used TPMS calcium phosphate implants [88]. The TPMS implants can significantly enhance the new bone formation performance. TPMS architectures have generally been confirmed to be a perfect fit for biological applications. It is possible to create exceptional TPMS scaffolds

or implants with appropriate geometries and performances to satisfy the requirements of the real biological environment of humans.

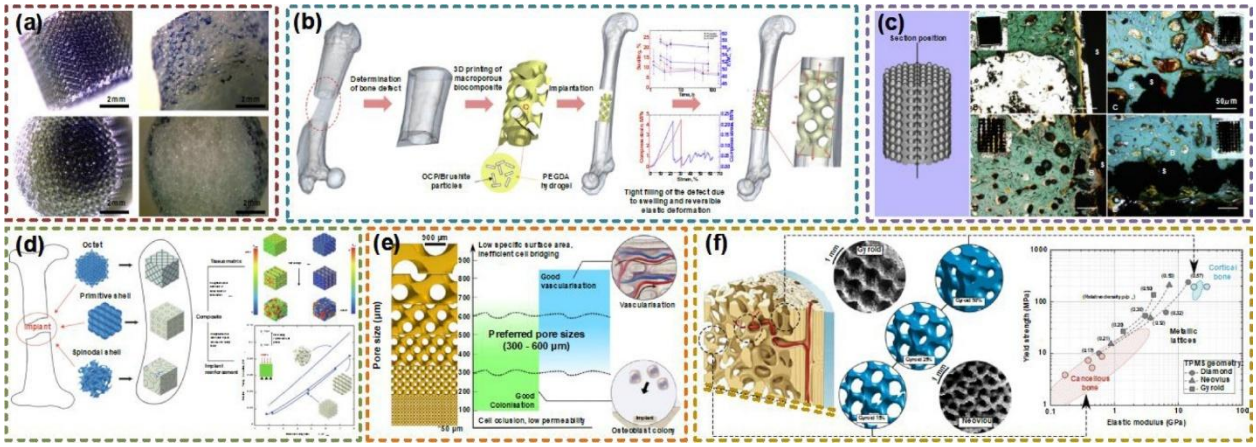

Figure 7. applications of TPMS structures in biology. (a) Salt-leached scaffolds combined with TPMS [81]. (b) TPMS is utilized to fill up bone defects [82]. (c) TPMS scaffold histological findings [83]. (d) Lattice and TPMS scaffold comparisons [84]. Preferred TPMS pore sizes for different bone stages [85]. TPMS metallic bone [86]. [43]

1.2.3. Gyroid

In several engineering applications, lattice structures have proven to offer exceptional mechanical properties, enhancing stiffness, strength, toughness, and crashworthiness [89-91]. defined by minimized local area, where every patch extracted from the TPMS that is considered small enough has the smallest area of all patches created within the same borders [92]. This structure separates the space into two congruent, linked zones and is made up of smooth, continuous surfaces that are infinitely extended in the volume. Shoen [93] was among the first to investigate TPMS-gyroid, demonstrating their prospective multifunctional structure for a variety of uses, such as heat exchanges, sound control, and impact absorption.

The mechanical response of the TPMS-gyroid structures was examined in a number of numerical and experimental investigations. The compressive failure mechanisms and energy absorption of double gyroid structures made with SLM AlSi10Mg were investigated by Maskery et al. [94]. Based on their results, double gyroid lattices are suitable, achieving 16×10^6 Jm^{-3} specific energy absorption during compressive deformation up to 50% strain. Using quasi-static compression tests, Wang et al. [95] examined the 304 stainless steel SLM gyroid lattice structure, examining the absorbed energy and deformation modes. During compression, a steady and progressive buckling collapse was seen, and a parametric analysis showed that relative density had an impact on crushing load and absorbed energy. The mechanical response of gyroid lattice structures under a broad variety of volume fractions at various build orientations was assessed by Yan et al. [96, 97]. According to their findings, the lattice structures' compressive strength rose as the volume fraction increased. Gyroid structures with various lattices were compared by Li et al. [98] at quasi-static loading [99]. Their findings demonstrated the potential use in protective constructions by showing that the gyroid lattice structures with relative densities of 20% and 30%

absorb more energy per unit mass than the other structures (i.e., Diamond, Gyroid, IWP, and Primitive). Abueidda et al. [92, 100] examined the energy absorption, compressive strength, and uniaxial modulus of gyroid structures and contrasted them with several TPMSs, including Primitive, Neovius, and IWP. According to their findings, gyroid structures outperform other lattice structures in terms of mechanical qualities. These studies show that gyroid lattices are appropriate for energy-absorbing applications. However, given the current lack of information, the fascinating application of gyroid lattices necessitates further research in extreme applications where materials and structures were subject to high strains and strain rates, such as in armored panels and helmet protective padding.

In the following Figure (Figure 8) you are observing the isosurface, FE mesh, and manufactured sample used Gyroid structure. The Gyroid unit cell is governed by the following mathematical equation:

$$\sin(\frac{2\pi}{a}\cdot x)\cos(\frac{2\pi}{a}\cdot y)+\sin(\frac{2\pi}{a}\cdot y)\cos(\frac{2\pi}{a}\cdot z)+\sin(\frac{2\pi}{a}\cdot z)\cos(\frac{2\pi}{a}\cdot x)=t \quad (1)$$

where constants *a* and *t* control the unit cell size and the volume surrounded by the Gyroid surface.

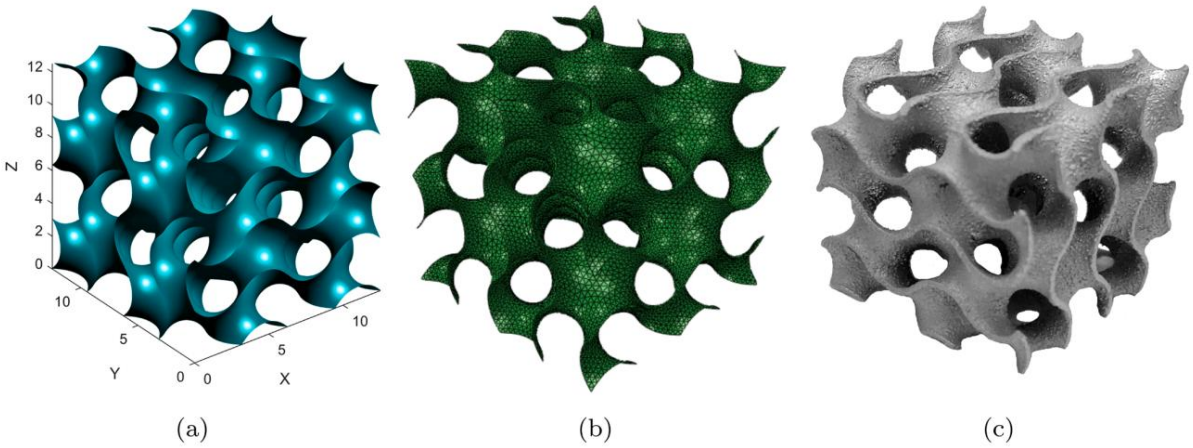

Figure 8. Gyroid (a) isosurface, (b) FE mesh, and (c) manufactured sample [101].

This research focuses on a specific TPMS lattice architecture named as FRD and compares its mechanical performance with two other widely studied TPMS topologies: the Gyroid and Fischer–Koch–S structures. To investigate the influence of VF distribution and geometric grading, three FRD configurations were designed: a uniform lattice with a constant VF of 45% (FRD-45), and two functionally graded versions—FRD-30 (graded from 30% to 60%) and FRD-40 (graded from 40% to 50%). For Comparison, the Gyroid and Fischer structures were also fabricated with a uniform VF of 45%, referred to as Gyroid-45 and Fischer-45, respectively. This study's main goal is to assess and contrast these designed lattices' structural integrity, elastic stiffness, and energy absorption capacities under compressive loading. To thoroughly evaluate the mechanical response and failure behavior of these additively built structures, a thorough experimental approach that

included quasi-static compression testing, XCT characterization, fracture surface analysis and finite element simulation was used.

2. Materials and methods

2.1. Design and manufacturing of uniform and graded lattice structure

Figure 9 illustrates that the engineered lattice structures have unit cells of 4 mm in length, systematically organized in a 5 × 5 × 5 arrangement, yielding ultimate dimensions of 20 mm × 20 mm × 20 mm. These constructions are intended to examine the impact of unit cell variation on mechanical performance and functioning.

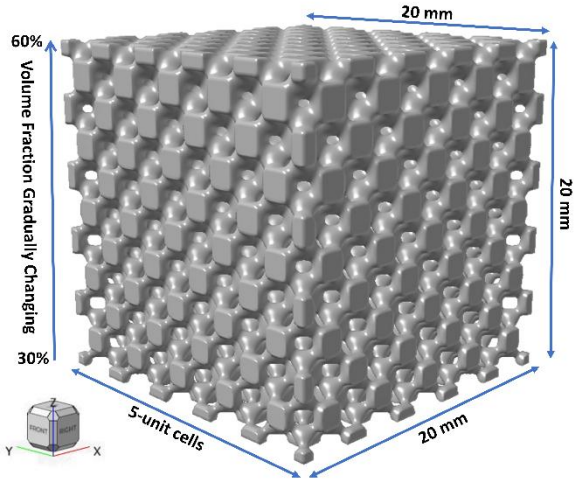

Figure 9. TPMS Geometry

Both the GLS and the uniform lattice structure (ULS) possess an overall VF of 45%.. While the ULS maintains a uniform VF throughout the structure, the GLS shows a progressive fluctuation in VF from 30% to 60% and from 40% to 50% along the Y-axis. This gradient is attained by methodically altering the geometric characteristics of the unit cells in a regulated manner, enabling a spatially optimum material distribution.

In this study, the material selected for specimen fabrication is the AlSi10Mg aluminum alloy (Figure 10). Commercial aluminum alloys, including near eutectic Al-Si alloys like AlSi10Mg, Al-12Si, A357, and A356, are typically utilized in AM processes, especially L-PBF. Of these, AlSi10Mg is undoubtedly the composition that has been investigated the most [33, 102-105]. The Si content, which is near the eutectic one and prevents the solidification cracking phenomenon, is primarily responsible for this composition's success. This breaking mechanism is known to be associated with the alloy's solidification range, fluidity of the molten phase, solidification shrinkage, and coefficient of thermal expansion (CTE) [106]. The fine solidification range ($\Delta T = T_{liquidus} - T_{solidus}$) of AlSi10Mg, which was estimated to be around 30 °C, is implied by the presence of 10 weight percent Si [107]. Compared to other high strength aluminum alloys, like the 2024 (ΔT = 135 °C), this value is incredibly low [108]. Furthermore, it is well known that Si decreases the coefficient of thermal expansion, solidification shrinkage, and enhances the fluidity of molten aluminum [108]. Additionally, as Si is in charge of laser absorption, Sercombe et al. proposed that it is also essential for the AlSi10Mg L-PBF processing. In actuality, silicon is not soluble in Al and is mostly present in the alloy as pure particles with a high (~70%) laser absorption [109]. The

material compositions and properties of AlSi10Mg used in this work are summarized in Table 1 and Table 2.

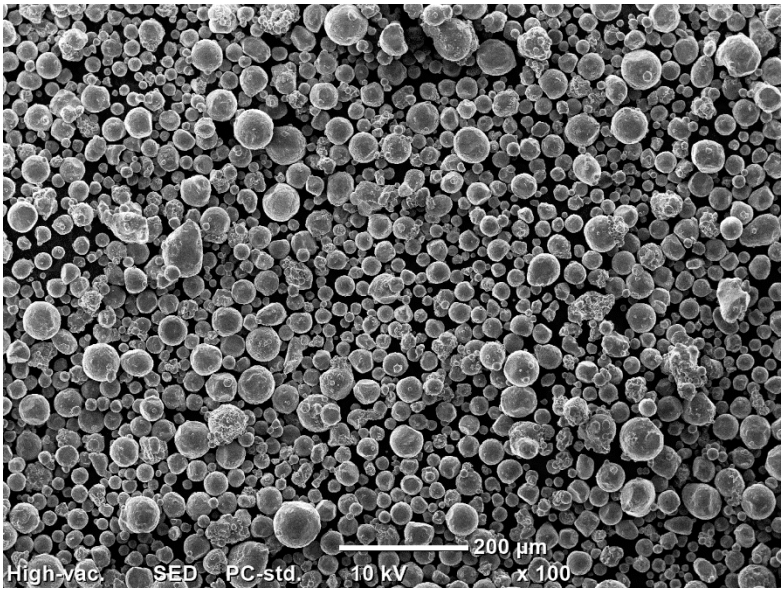

Figure 10. AlSi10Mg Powders used in this study.

Table 1. Chemical Composition of AlSi10Mg Powders

Elements	Al	Si	Fe	Cu	Mn	Mg	Ni	Zn	Pb	Sn	Ti
Wt%	Balance	9.0–11.0	< 0.55	< 0.05	< 0.45	0.25–0.45	< 0.05	< 0.10	< 0.05	< 0.05	< 0.15

Table 2. Material properties of the AlSi10Mg Aluminum alloy [110].

Property	Value (Std. Dev.)
Density [g/cm³]	2.69 (0.05)
Young's modulus [GPa]	76 (5)
Yield stress [MPa]	225 (5)
Ultimate strength [MPa]	441 (7)
Ultimate strain [–]	0.040 (0.002)

In recent years, a lot of research has been done on the microstructure and characteristics of AlSi10Mg via L-PBF [102, 111]. It is widely acknowledged that the as-built AlSi10Mg L-PBF microstructure is composed of massive columnar grains that are hundreds of microns long and 10–

20 microns wide (Figure 11a). These grains are created during the building process as a result of the epitaxial grain growth along the building direction; they are only detectable by electron backscatter diffraction (EBSD) investigations. It is commonly recognized that the quick and directed cooling that occurs during laser scanning gives these huge columnar grains their fine dendritic structure, which suggests improved mechanical qualities. A chain of connected melt pools with incredibly small cellular structure can be used to identify the influence of laser scanning in optical or scanning electron microscopy (SEM) pictures. The building characteristics and the location inside the melt pool have a significant impact on the size and shape of the cells [107, 112]. For instance, Kim et al. identified three distinct melt pool regions—the fine melt pool (FMP), heat affected zone (HAZ), and coarse melt pool (CMP)—that are separated by cells of varying sizes and shapes (Figure 11b) [112]. This cellular structure is composed of Al cells encircled by Si-rich regions, according to Energy-dispersive X-ray spectroscopy (EDS) analysis (Figure 11c–e).

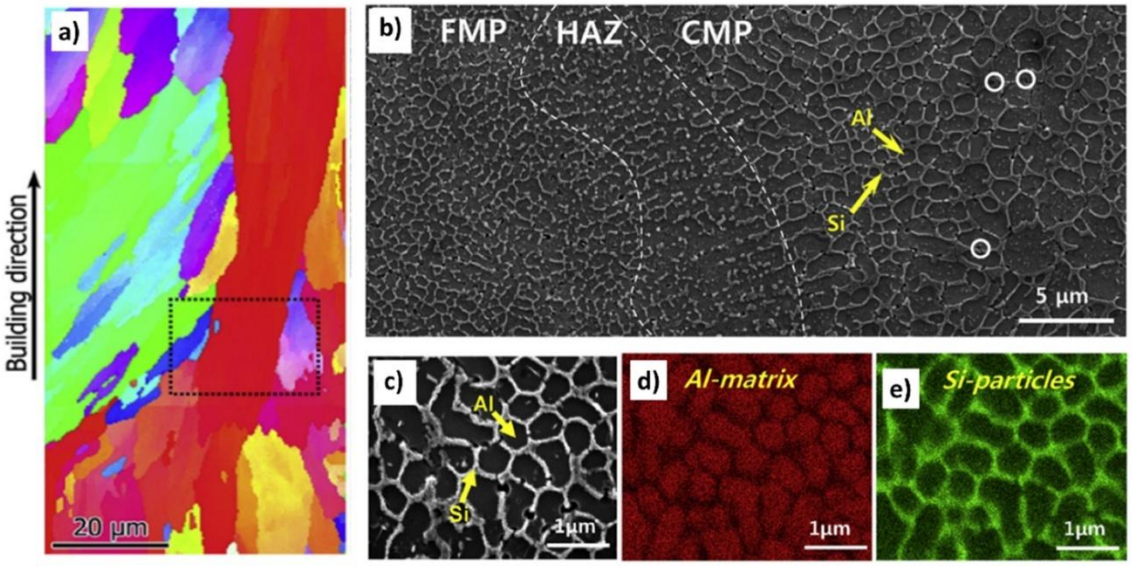

Figure 11. (a) Inverse pole figure (IPF) for electron backscatter diffraction (EBSD), modified from [113], An as-built AlSi10Mg sample's (b,c) SEM pictures and (d) Al- and (e) Si EDS maps were taken from [112].

The graph presented below (Figure 12) provides a comprehensive visualization of the various lattice structures that were designed using the Altair Inspire application (Figure 13). These structures were accurately developed to explore their mechanical performance and manufacturability in the context of AM. At the bottom section of the figure, the corresponding additively manufactured samples produced via L-PBF are depicted.

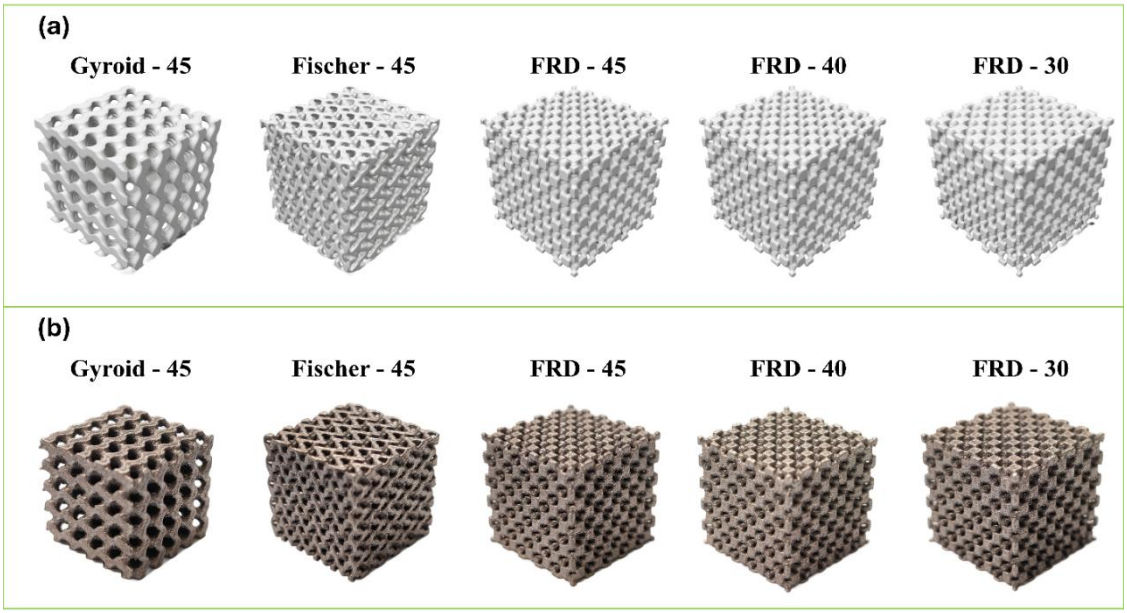

Figure 12. STL files extracted from CAD software (a), and the as-built structures (b).

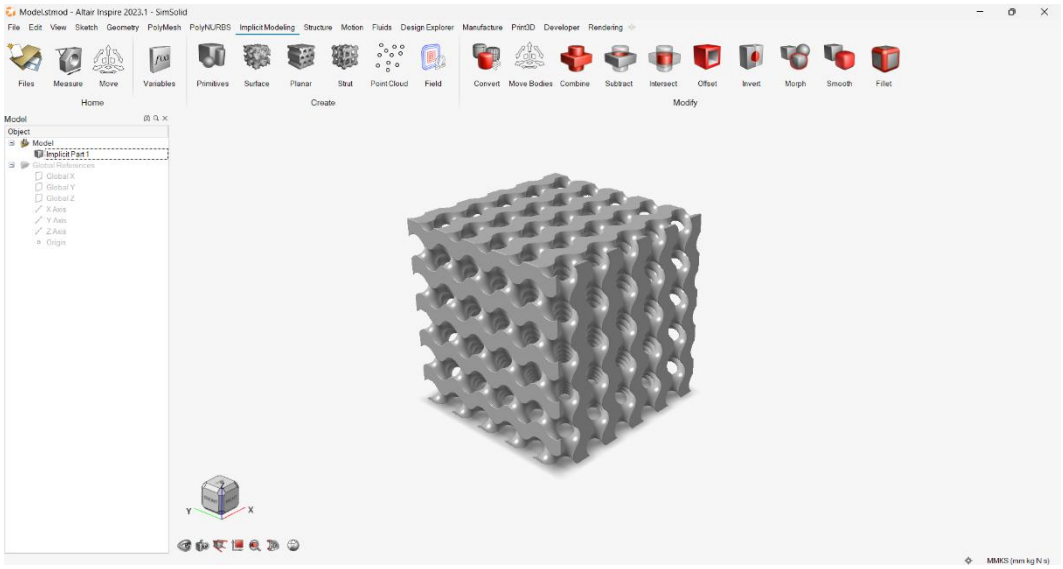

Figure 13. Designing TPMS structures in Altair Inspire 2023.1.

2.2. L-PBF

The L-PBF production process was executed with the Print Sharp 250 machine (Prima Additive)(Figure 14)(Table 3). Before printing, the STL files of the proposed lattice structures were generated and then carefully placed on the build platform using Materialise Magics, which enabled optimum positioning and orientation of the samples to improve printability and minimize support material needs (Figure 15). The slicing and parameter assignment for fabrication were performed using EPHatch, with the optimum process settings shown in Table 4 setup for the Print Sharp 250 machine. Mercurio V. et al [114] by varying different parameters such as Scanning Speed, Hatching Distance, Laser Power, and Scanning Speed found out that utilizing the parameters described in Table 4 will results in density of 99.80% with few irregular pores (Figure 16). For the given parameter set, a rotating stripes scan approach with a rotation angle of 67° in each layer is employed to decrease residual stress and anisotropy. The build platform's pre-heating temperature was raised to 100 °C in order to enhance thermal conductivity and powder layer melting [114](Figure 17).

Figure 14. Print Sharp 250 machine.

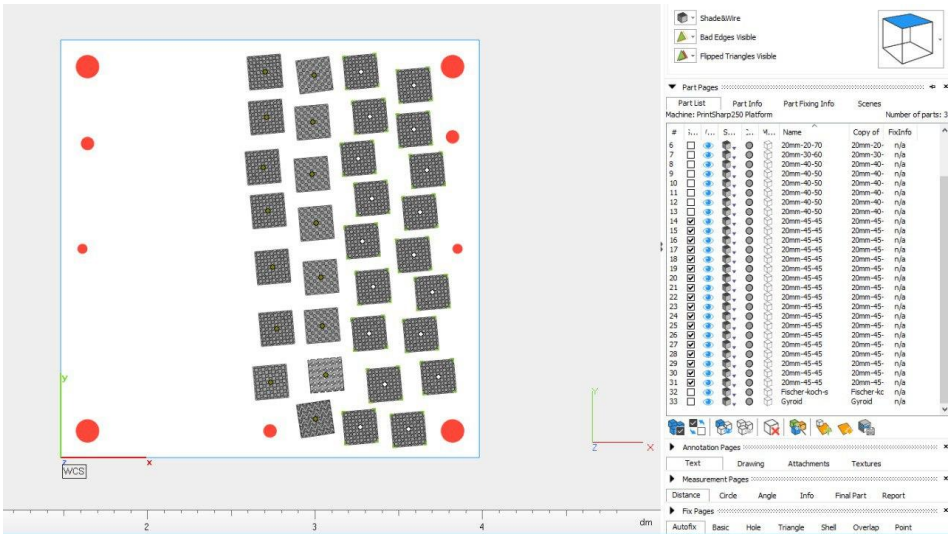

Figure 15. Optimized Arrangement of Lattice Samples on the Build Platform Using Materialise Magics to Enhance Printability and Reduce Support Material Requirements.

Table 3. The technical parameters of PrintSharp 250.

Category	Specification
Dimensions (L.W.H)	3500 (L)–1100 (W)–2450 (H) mm
Weight	2000 kg
Power Supply	380 V/50 Hz/8kW
Type of laser	Yb (Ytterbium) Fiber Glass
Laser Power	200 W/ 500 W (Optional)
Laser Focus Diameter	70 – 100 µm
Beam Wavelength	1060 – 1080 nm
Building Volume	250 x 250 x 300 mm
Beam Deflection Speed	8 m/s
Positioning Speed	10 m/s
Build rate	12 – 30 cm^3/h
Layer Thickness	0.02 – 0.1 mm
Layer Width	0.1 mm (single line width)
Recoater Specs	Travel: 650 mm
Building Platform z-axis	Travel: 300 mm/Speed max: 6 mm/s/Res: 0.01 mm
Heating Platform	Up to 200°C
Monitoring of O_2 Level	Below 100 ppm
Permissible Room Temperature	15 – 30°C
Gas (Consumption – running/filling)	7 l/min (running)
System Fill Consumption	20 l/min (up to filling)
Cam Software	Materialise Magics
Control & Other Software	Eplus control software (EPC)
Industrial Interfaces	Ethernet

Table 4. L-PBF parameters used in this work to print the structures.

Laser Power [W]	370
Scanning Speed [mm/s]	1400
Hatch Spacing [mm]	0.13
Hatch Rotation Angle [°]	67
Hatch Order Type	Discontinues
Layer Thickness [mm]	0.030

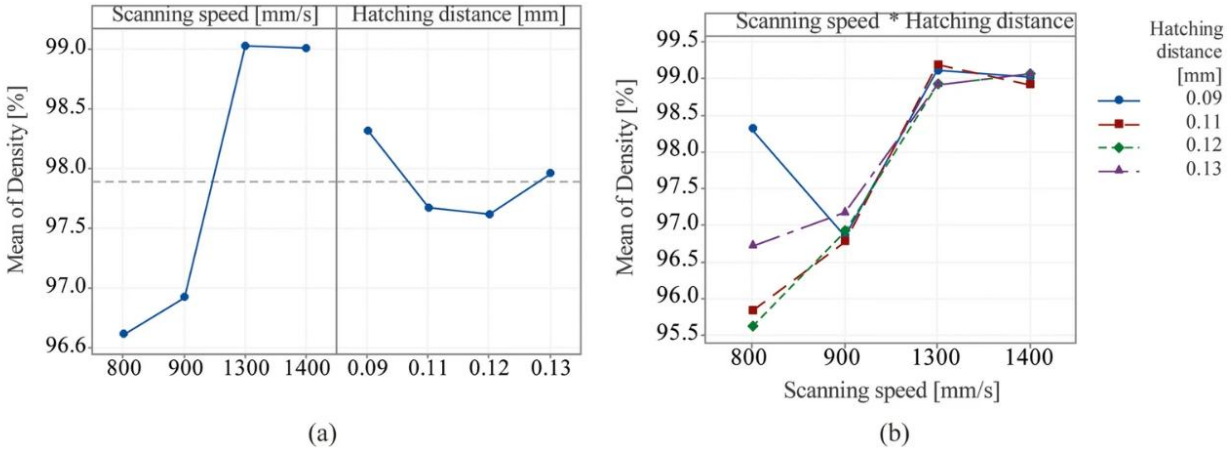

Figure 16. AlSi10Mg components produced sustainably using a L-PBF process [114].

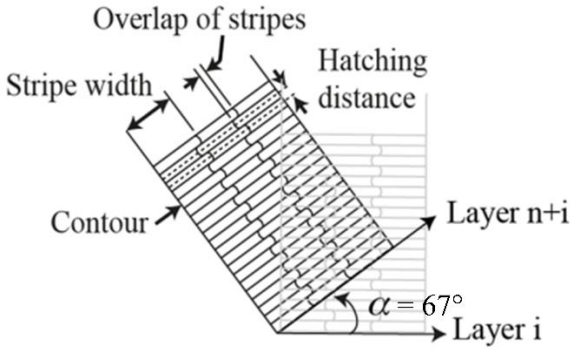

Figure 17. Hatch angle rotating in order to decrease residual stress and anisotropy.

Volumetric energy density (VED), a useful term that measures the amount of input energy per unit volume of the powder bed, varied significantly as a result of the wide range of factors. The idea of VED was initially introduced in references [115, 116] to compare the various sets of parameters in order to achieve significant relevance. The relative density of materials processed with L-PBF is assessed using VED, which is referenced in Eq. 2 of this thesis [117].

$$VED = \frac{P}{V \times h \times l} \tag{2}$$

Where:

$$\text{VED} = \text{Volumetric Energy Density } [\frac{J}{mm^3}]$$

$$P = \text{Laser Power } [\frac{J}{s}]$$

$$V = \text{scanning speed } [\frac{mm}{s}]$$

$$h = \text{Hatching distance [mm]}$$

$$l = \text{Layer thickness [mm]}$$

Subsequently, in our case the VED was determined to be 67.76 $\frac{J}{mm^3}$.

The chosen fabrication settings were intended to guarantee superior geometric accuracy, efficient material consolidation, and the reduction of prevalent flaws associated with L-PBF, including internal porosity and residual stress. After the printing procedure, the samples were meticulously detached from the build plate using wire electrical discharge machining (W-EDM). This post-processing approach was used to provide a precise separation with less mechanical stress, thereby preventing possible damage to the lattice structures that may arise from traditional cutting methods.

2.3. Wire Electrical Discharge Machining

At this stage, the G.cut W-EDM system was used to cut the samples. The equipment is depicted in Figure 18. Section 1 highlights the software interface of the machine, which controls wire movement, the automatic operation process, and the start/stop functions for cutting. Section 2 shows the X, Y, and Z axes, which help guide the cutting direction accurately. Section 3 is the core operational area where the workpiece is positioned and the cutting takes place.

Figure 18. Key components of the W-EDM machine: Section 1 (software controls), Section 2 (coordinate display), and Section 3 (cutting area).

To begin, the sample platform was secured to the W-EDM machine using clamps. Then, via the machine's dedicated software, a surface contact was made between the wire and the platform to define the reference point for both x and y axes. After setting the starting point, the correct dimensions and orientation were loaded into the system to initiate cutting.

The wire-cutting process relies on a thin, electrically charged wire that precisely slices through the material. This technique works by creating controlled electrical discharges—or sparks—between the wire and the workpiece, gradually removing material along the cut path. As shown in Figure 19, these sparks occur rapidly and remove tiny amounts of metal to form the desired geometry.

Figure 19. Illustration of electrical sparks and the movement of water during the wire-cutting procedure.

During the cutting operation, deionized water continuously circulates to cool both the wire and the workpiece, preventing overheating and flushing away debris. This water also acts as a dielectric medium, which is vital for enabling the discharge process. Two important parameters in this method are "time on" (T_{on}) and "time off" (T_{off}). T_{on} determines the duration and energy of each spark, influencing cutting speed and surface finish. T_{off} provides brief pauses between pulses, allowing for cooling and reducing thermal damage, which in turn improves cutting precision. These settings are crucial for optimizing cutting performance and achieving high-quality results [118]. After cutting, the fabricated components were removed and prepared for the next steps.

The following graph (Figure 20) depicts the three unique FRD lattice configurations used in this research. The top and middle models depict graded lattice systems, with volume fractions ranging from 30% to 60% and 40% to 50%, respectively. Conversely, the inferior model illustrates a homogeneous lattice configuration with a consistent volume proportion of 45%.

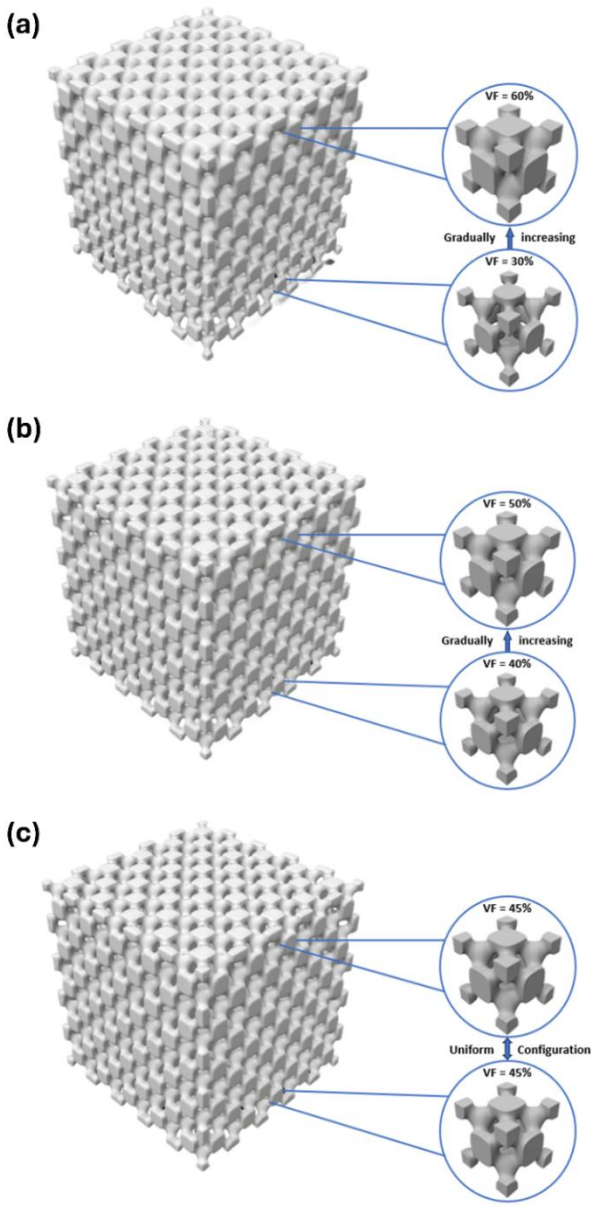

Figure 20. (a) FRD - 30 and (b) FRD - 40 are the GLSs designed and (c) is the ULS designed FRD.

3. Results and discussions

3.1. Quality Assurance

X-ray Computed Tomography (XCT) reconstructs 3D models by combining multiple X-ray images captured around a rotating axis [119]. Over time, three main XCT techniques have emerged, each improving data acquisition speed.

The first method captures density information using linear X-ray beams that move in the opposite direction of a detector. The scanner rotates incrementally until it completes a full 360° scan. The second method uses a 2D X-ray array spanning the object's width, paired with a 1D detector array located along the beam's edges. The third technique utilizes a cone-shaped 3D X-ray beam and a 2D detector. In this setup, the X-ray source and detector scan a cross-sectional slice along the xy-plane with minor vertical (z-axis) adjustments for full coverage. While fan beam scanners capture an entire slice at once, cone beam scanners can scan the entire object in one go. All scanning techniques involve a complete 360° rotation to capture the object [120]. Figure 21 shows each of the XCT techniques.

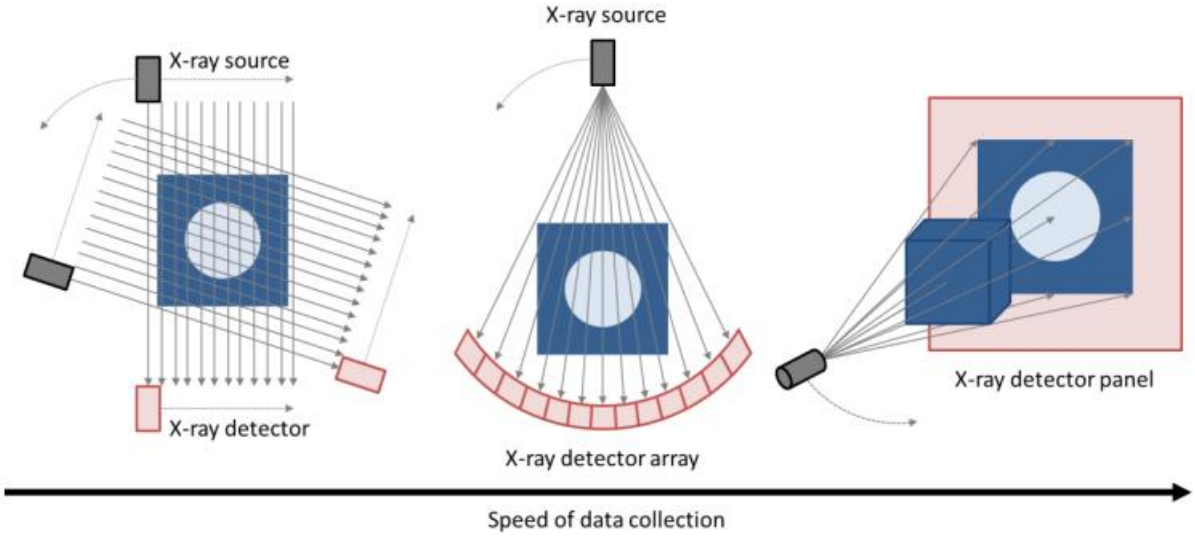

Figure 21. Diagrams for the fan, pencil, and cone beam XCT techniques, respectively. It should be mentioned that both curved and flat panel detector arrays can be utilized in this illustration, where the fan beam image shows a curved detector and the cone beam image shows a flat panel detector [121].

Following data collection using one of the previously described techniques, a computer system processes the data and uses the obtained x-ray intensity readings for each detector element to do a reconstruction. Individual linear attenuation coefficients added together along a vector across the measurand from the x-ray source to the detector element produce these intensity readings. The computer creates individual slice images using these data, which can subsequently be layered to create a three-dimensional reconstruction [121]. From straightforward visualization to precise geometry measurement or conversion into a.STL (STereoLithography) file [122] for AM production, the resulting 3D reconstruction can subsequently be used for several purposes.

Image quality in XCT—particularly resolution and contrast—is a key evaluation metric. As object size increases, magnification decreases due to reduced X-ray penetration, which in turn lowers image resolution. Lower magnification results in larger scan voxels and reduced image sharpness. Dense materials further complicate scanning due to poor X-ray penetration, requiring longer exposure times for sufficient contrast. To address this, XCT often focuses on scanning only a specific region or uses a reference sample with similar characteristics to enhance image clarity. However, while this targeted approach may improve image quality, it may fail to fully represent the object, potentially leading to inaccurate results.

A thorough quantitative analysis of manufacturing discrepancies was performed using Phoenix v|tome|x s XCT to guarantee an exhaustive examination of the produced lattice structures (Figure 22).The scanning process used a 180 kV X-ray source with a filament current of 60 µA, enabling high-resolution imaging. A DXR-250 RT detector was used to improve accuracy, with the focal spot size set at 10.8 µA, hence improving picture clarity and structural detail. A total of 1050 radiographic images were obtained at several angles, guaranteeing comprehensive coverage of the interior anatomy. The predicted voxel resolution of 35.26 µm enabled a thorough examination of minute aberrations and structural anomalies.

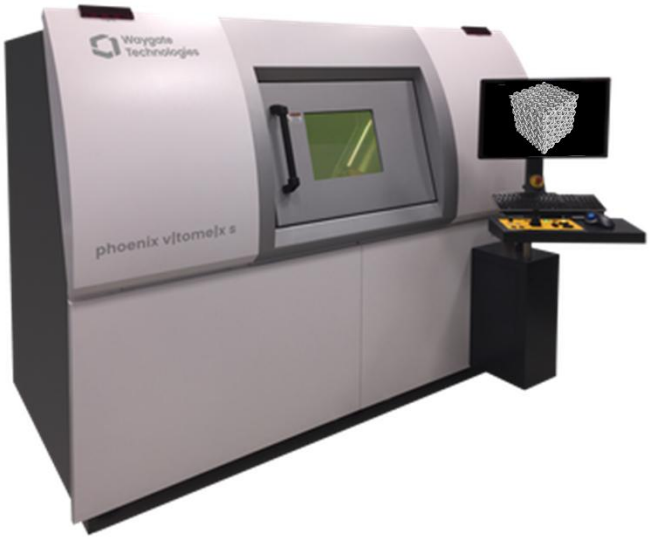

Figure 22. Phoenix v|tome|x s XCT.

Post-processing analysis and defect assessment were conducted using VG Studio MAX 3.1 software, a sophisticated three-dimensional visualization and measurement instrument. The VGDefX method was used to systematically identify and evaluate internal flaws, such as porosities, unmelted particles, and dimensional discrepancies inside the lattice structures. This method offered a thorough evaluation of geometric accuracy, pinpointing possible sources of variability and their effects on mechanical performance. To elucidate the results, the CT scan pictures were classified in the following figure, where transparency was adjusted to 85% to maintain the visibility of porosities while ensuring the structural integrity of the samples. The

distribution of porosity diameters is provided, yielding significant insights into defect dimensions and their prevalence.

This figure (Figure 23) presents a comprehensive XCT assessment of internal porosities within TPMS lattice structures manufactured via L-PBF. Subfigures (a), (b), and (c) illustrate orthogonal 2D cross-sectional slices along different planes of the FRD – 30 Structure, with each image mapping pore diameters using a calibrated color scale ranging from 0.28 mm (blue) to 0.61 mm (red). These maps provide spatially resolved visualization of pore distribution and size variation within the printed geometry.

The porosity diameters are color-coded and quantified to assess manufacturing quality, internal defect morphology, and potential correlations with mechanical performance. This XCT-based approach provides a non-destructive and high-resolution method for evaluating the internal integrity of lattice structures, crucial for load-bearing applications.

To facilitate internal porosity analysis, three orthogonal slice planes were generated across the lattice structure at different spatial positions relative to the origin. The XY plane, corresponding to the green slicing line, was positioned at –0.81 mm from the origin, allowing visualization of horizontal pore distribution. The YZ plane, shown in blue, was sectioned at +5.65 mm, providing a longitudinal view through the depth of the structure. Lastly, the XZ plane, indicated by the red slicing surface, was located at +0.46 mm from the origin, enabling the examination of vertical porosity gradients. These precisely positioned slices ensure comprehensive spatial coverage of internal defects and facilitate accurate quantitative assessment of pore diameters throughout the lattice volume.

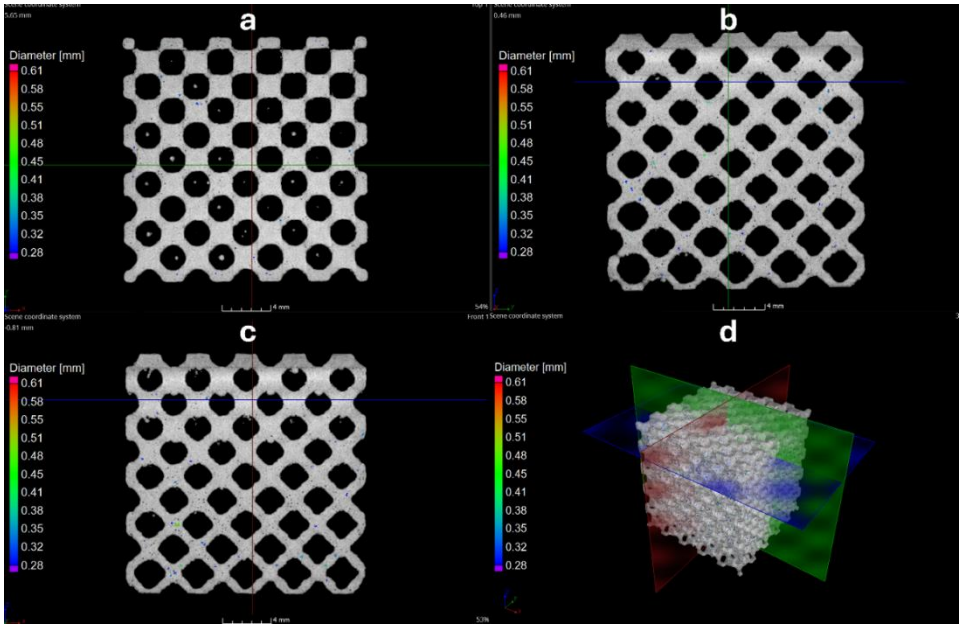

Figure 23. 3D XCT-Based Porosity Diameter Mapping in Additively Manufactured FRD - 30 TPMS Lattice Structure with Orthogonal Slice Views.

This figure (Figure 24) compares the internal porosity distribution of two FRD lattice structures—FRD-30 (left) and FRD-45(right)—using 3D reconstructions obtained from XCT. The color map indicates pore diameters ranging from 0.28 mm (blue) to 0.61 mm (red), allowing for a quantitative and spatial comparison of pore morphology within the structures.

In the FRD-30 sample, a denser and more widespread presence of small- to medium-sized pores is observed, with color-coded pores predominantly appearing in green and cyan, suggesting greater porosity content and variability across the structure. In contrast, the FRD-45 sample exhibits fewer pores, primarily in the blue to light-blue range, indicating smaller pore diameters and reduced overall defect content. Importantly, red-colored pores—representing the largest defect sizes—are sparsely distributed and occur predominantly near the outer surfaces of both structures., confirming that extreme porosity is not a dominant issue in either case. The pore segmentation is overlaid on the as-built structure geometry to visually correlate internal defect morphology with the surrounding lattice architecture, offering insight into how gradient design impacts pore distribution during the L-PBF process.

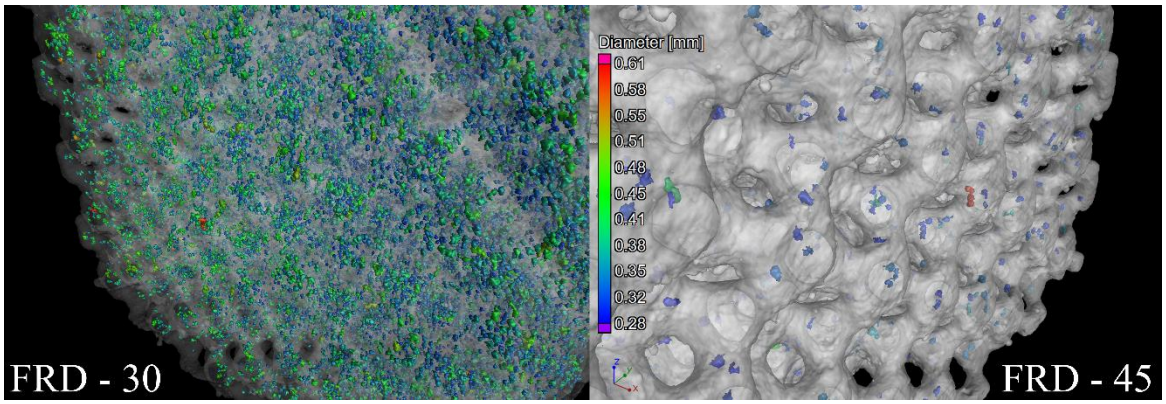

Figure 24. 3D XCT-Based Porosity Visualization of FRD-45 and FRD-30 Structures Showing Limited Presence of Large-Sized (Red) Defects.

The image below (Figure 25) presents a detailed analysis of a Gyroid TPMS lattice structure using CT. Subfigure (a) displays the 3D as-built geometry of the lattice, revealing the complex, periodic surface architecture characteristic of the Gyroid topology. Subfigure (b) overlays CT-based porosity mapping onto the lattice structure, with color coding representing pore diameters ranging from 0.28 mm to 0.75 mm. This enables spatial localization and qualitative evaluation of internal defect distribution. Subfigure (c) shows a quantitative defect histogram extracted from CT data, highlighting the frequency and distribution of pore diameters within the structure. A marked value of 0.20 mm is indicated, suggesting a concentration of small-diameter pores. This analysis provides valuable insight into the internal quality, porosity morphology, and overall manufacturing precision of the Gyroid structure fabricated via additive manufacturing.

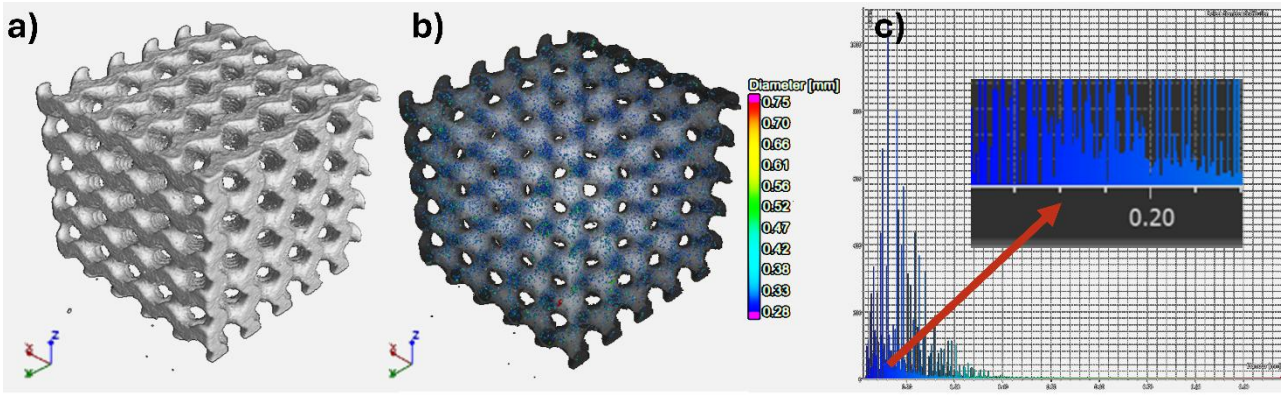

Figure 25. XCT-Based Analysis of a Gyroid TPMS Lattice Structure: (a) As-built geometry, (b) 3D porosity mapping with color-coded pore diameters, and (c) histogram showing pore diameter distribution with dominant value at 0.20 mm

Additionally, essential volumetric parameters—comprising Material Volume (mm^3), Defect Volume (mm^3), and the Defect Volume Ratio—were calculated and shown in the following table (Table 5). These values provide a quantitative assessment of defect content, enabling a more profound examination of their possible impacts on the mechanical characteristics of lattice systems. This innovative characterization technology enhances additive manufacturing processes and provides essential insights into defect development mechanisms and their impact on structural integrity.

Table 5. Quantitative Analysis of Material and Defect Volume in Different Lattice Structures

	Fischer	Gyroid	FRD – 45	FRD – 40	FRD – 30
Material Volume [mm^3]	3715	3488	4075	3871	3852
Defect Volume [mm^3]	22.63	31.91	27.90	43.74	57.40
Defect Volume Ratio [%]	0.61	0.91	0.68	1.13	1.49

The Figure 26 illustrates the variation in void fraction among different TPMS lattice structures. As shown, the Gyroid topology exhibits the highest void fraction, measured at 56.40%, indicating a relatively more open and interconnected architecture compared to the other examined structures. This elevated level of voids is expected to significantly influence the mechanical behavior, energy absorption capacity, and mass efficiency of the lattice, making it a promising candidate for applications requiring lightweight yet mechanically responsive materials.

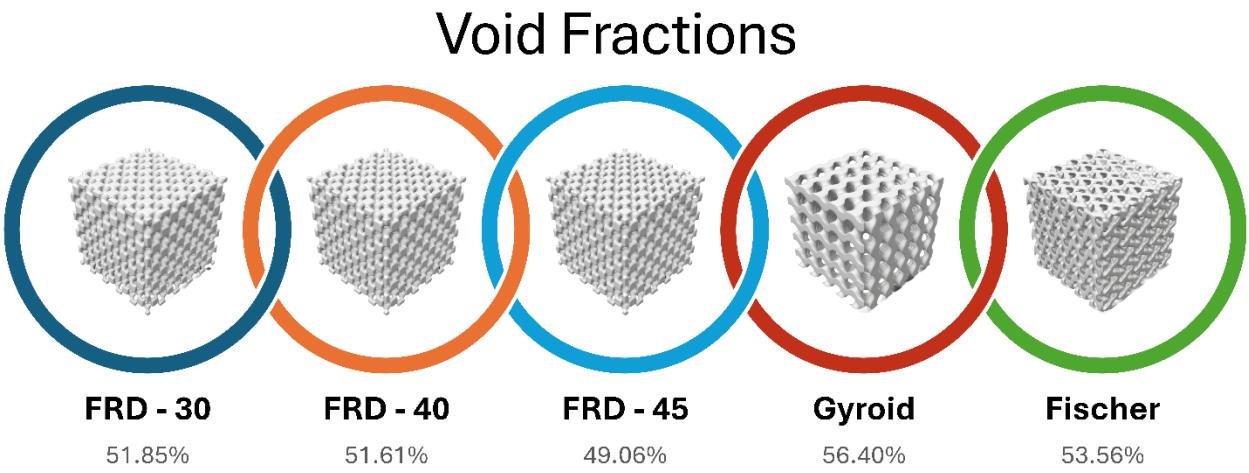

Figure 26. Void Fractions for different TPMS structures.

The comparison between the CT-reconstructed volume and the corresponding engineering design, as illustrated in Figure 27, corroborates the presence of manufacturing-induced deformations. These discrepancies are predominantly to suboptimal thermal management in cantilever regions, where inefficient cooling during the additive manufacturing process exacerbates geometric inaccuracies[123].

In the second column of the figure, the deviation distribution across the surface area is presented, quantifying the local discrepancies between the fabricated and designed geometries. The maximum deviations, expressed in millimeters, were observed as follows: Fischer (-0.02 mm), Gyroid (0 mm), FRD - 30 (-0.01 mm), FRD - 40 (-0.03 mm), and FRD -45 (-0.04 mm). These values indicate that while the Gyroid structure closely adheres to its intended geometry, the FRD-graded designs, particularly FRD-45, exhibit more pronounced deviations. This trend further emphasizes the impact of gradient complexity on dimensional accuracy in L-PBF processes.

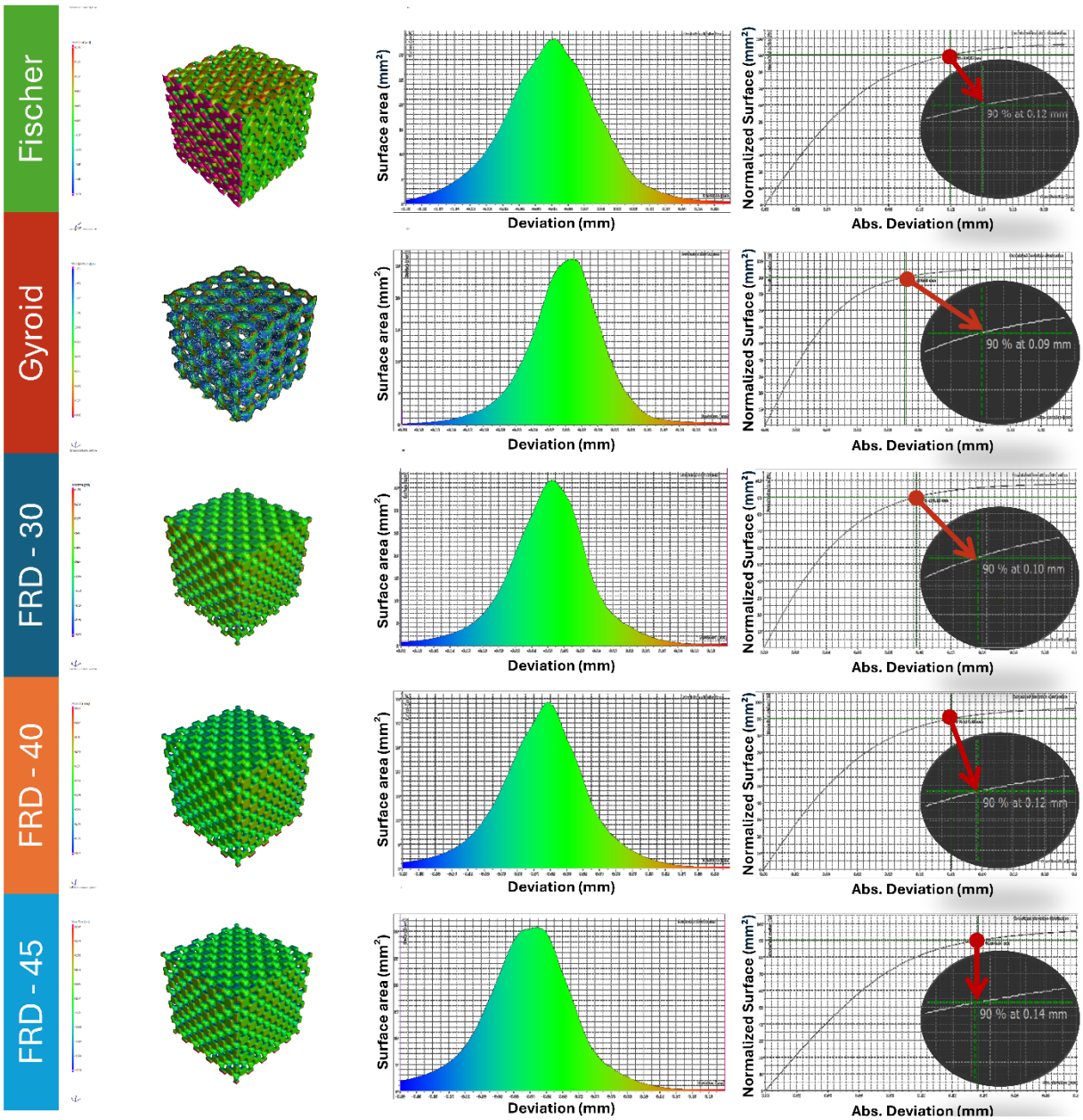

Figure 27. CT data analysis for the as-built TPMS structures.

3.2. Compression Test

To evaluate and compare the energy absorption capacity of various TPMS lattice structures, quasi-static compression tests were conducted in accordance with the ISO 13314 standard. This standard requires testing a minimum of three specimens per configuration to ensure statistical reliability. The experiments were performed using a displacement-controlled method at a constant rate of 5 mm/min, thereby maintaining consistent loading conditions across all samples. A pre-load of 1000 N was applied before testing to ensure proper contact between the compression plates and the specimen, thereby minimizing any initial misalignment effects (Figure 28–Figure 29). All tests were carried out using the Aura Universal Testing Machine (Easydur S.r.l., Italy), which provides high precision and stability for the mechanical characterization of lattice structures. This standardized testing procedure facilitates a reliable and reproducible comparison of the mechanical behavior and energy absorption performance of the studied TPMS architectures.

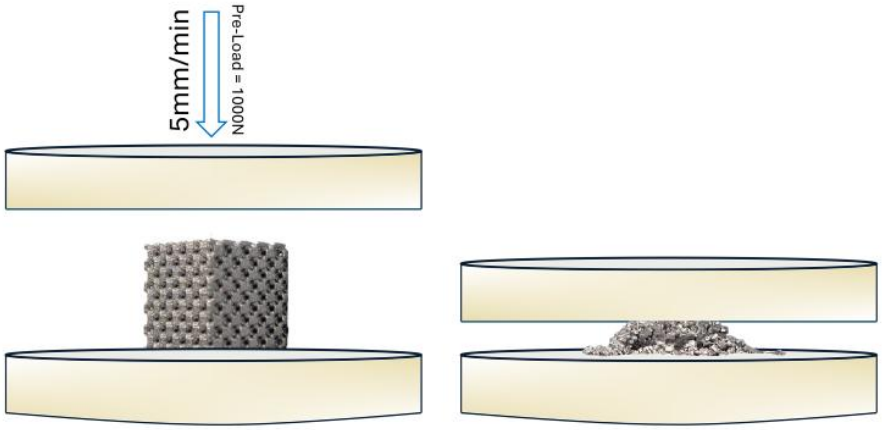

Figure 28. Quasi-Static Compression test.

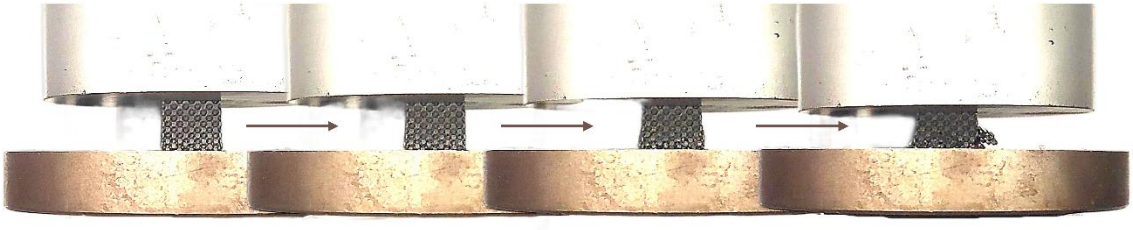

Figure 29. Compression Test process.

The Figure 30 presents the stress–strain behavior of lattice structures under uniaxial compression, accompanied by images that capture the evolution of its deformation. Initially, the stress–strain curve exhibits a linear trend that corresponds to the elastic response of the material, during which the lattice maintains its structural integrity. As the deformation progresses, the curve reaches a peak and then transitions into a plateau phase, reflecting the onset of plastic deformation characterized by localized nodal changes and the formation of shear bands, as evidenced by the images. Further along the curve, an increase in stress indicates the densification phase, where the structure compacts and significant fragmentation becomes apparent. Overall, the figure effectively correlates the mechanical performance with the observable physical changes in the lattice throughout the compression test for TPMS structures.

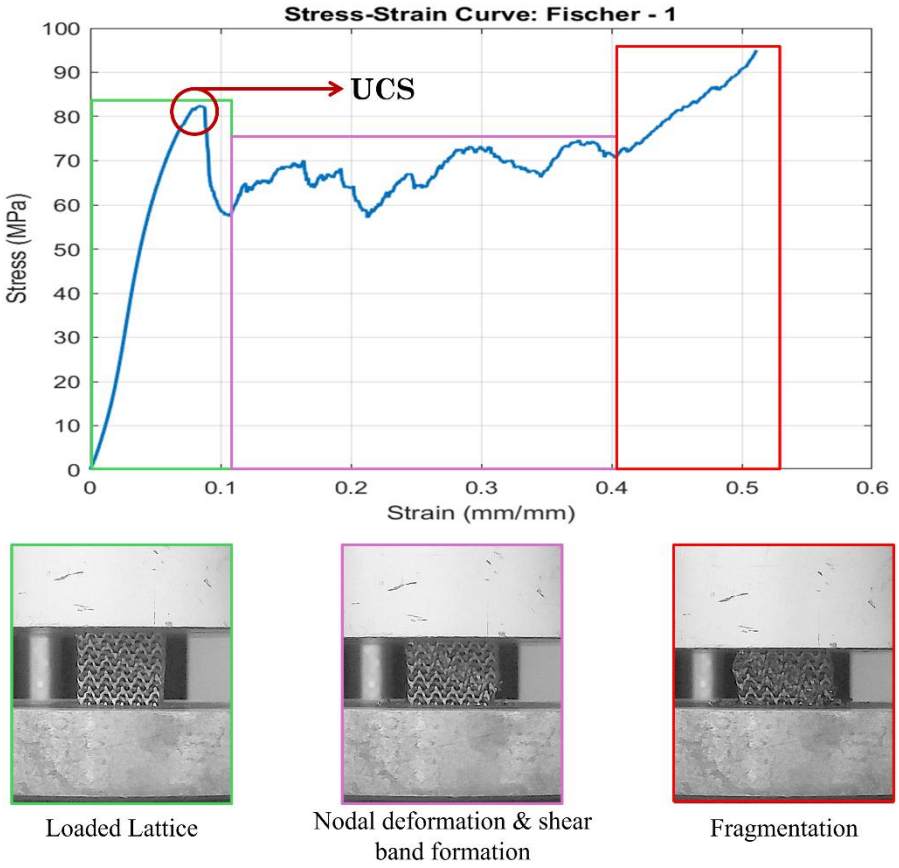

Figure 30. Failure modes and stress–strain curves.

The maximum load for the test was set at 38,000 N, as a sudden increase in force was observed, indicating that the structure had reached its failure point and experienced crumpling. The collected experimental data was subsequently analyzed using MATLAB, from which relevant graphs were extracted to illustrate the mechanical response of the TPMS structures under compressive loading. This analysis provides insights into the structural behavior and energy absorption characteristics of the tested samples.

3.3. Mechanical properties

This Figure (Figure 31) presents a detailed analysis of the mechanical response and energy absorption of various lattice structures under compressive loading. The force-displacement curves depicted in the first five subfigures illustrate the mechanical behavior of different lattice configurations, each subjected to quasi-static compression. These graphs provide insight into the elastic deformation, progressive collapse, and densification phases of the structures, which are critical for assessing their load-bearing capacity and energy dissipation efficiency.

The individual force–displacement graphs collectively illustrate the mechanical performance of various lattice designs under compressive loading. The first graph depicts the response of a gyroid-based lattice structure, revealing a characteristic pattern of stress accumulation followed by load redistribution, indicative of its complex deformation behavior (a). The second graph corresponds to the uniform FRD structure with volume fraction of 45%, which exhibits a clear progression of collapse and a defined post-yield behavior, reflecting its capacity to absorb energy through controlled deformation (b).

The third subfigure illustrates the force–displacement characteristics of a Fischer-based lattice structure, emphasizing its mechanical response during compression and the distinctive features of its failure mechanism (c). The fourth graph represents a graded lattice with a volume fraction gradient ranging from 30% to 60%, highlighting how functional grading enhances the structure's resilience and delay in failure onset (d). Lastly, the fifth graph shows the behavior of a graded lattice with a volume fraction variation between 40% and 50%, demonstrating a smooth response to external loading and revealing the influence of gradual porosity changes on its mechanical stability (e).

The final subfigure (f) quantitatively compares the absorbed energy for each lattice configuration, measured in joules (J). This 3D bar chart categorizes the total energy absorption of multiple specimens within each lattice type, enabling a comparative assessment of their impact resistance and energy dissipation efficiency. The results indicate significant differences in energy absorption, emphasizing the role of geometric design and volume fraction distribution in determining structural performance.

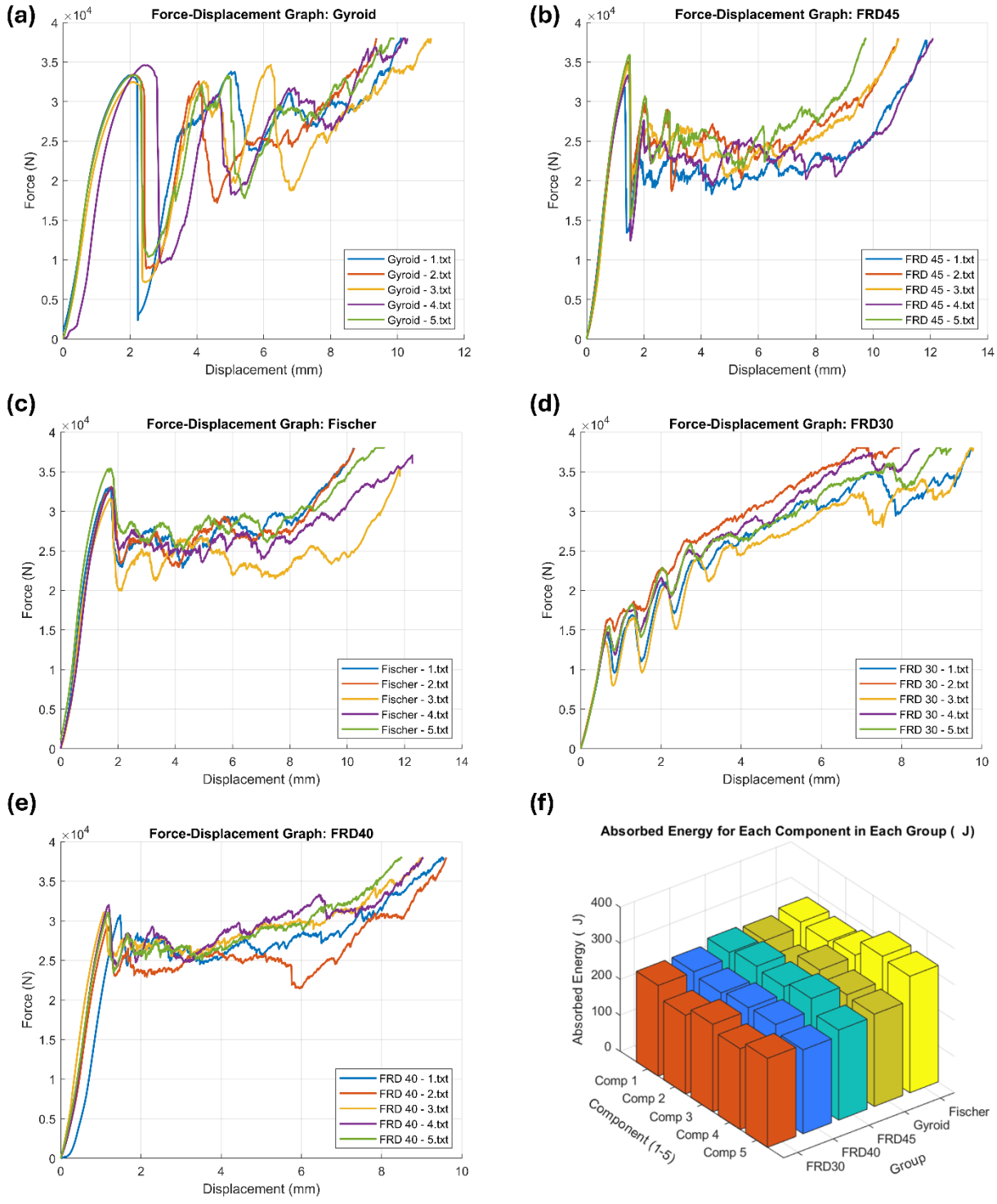

Figure 31. Force-Displacement Curves achieved by compression test (a-e), and the resultant absorbed energy for each sample (f).

The results are presented in the following graphs, providing a visual representation of the energy absorption characteristics of the tested structures. Finally, the average absorbed energy was calculated and is shown in the last graph (Figure 32). As depicted, the Fischer-Koch S structure exhibited the highest energy absorption capacity, absorbing 296.40 J. This was followed by FRD 45, Gyroid, FRD 40 and FRD 30, which absorbed 270.95 J, 257.67 J, 246.29 J, and 236.71 J, respectively. These findings highlight the variations in energy absorption efficiency among different TPMS structures, offering valuable insights into their potential applications in impact-resistant and energy-dissipative designs. Finally, specific absorbed energy, absorbed energy over mass, is illustrated in Figure 32-a, the average absorbed energy for each group is shown in Figure 32-b, and the resultant data is tabled in Table 6.

Table 6. Data related to the Absorption capacities of the structures.

Model	Mass [kg]	Average Absorbed Energy [J]	Average Specific Absorbed Energy [J/kg]
Fischer-Koch-S	0.0102	296.40	29058
Gyroid	0.0096	257.67	26840
FRD – 45	0.0104	270.95	26052
FRD – 40	0.0104	246.29	23682
FRD – 30	0.0104	236.71	22761

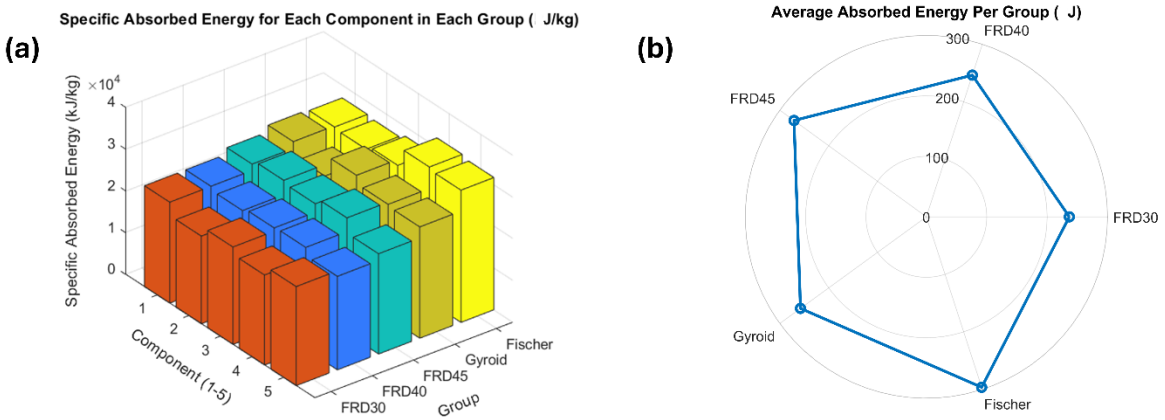

Figure 32. Specific Absorbed Energy for each group (a), and Average absorbed Energy per each group (b).

Furthermore, the stress–strain curves were analyzed to determine the Ultimate Compressive Strength (UCS) and elastic modulus for each structure. As illustrated in the corresponding figure, the average UCS values were found to be 38 MPa, 76 MPa, 85 MPa, 81 MPa, and 82 MPa for the FRD 30, FRD 40, FRD 45, Fischer, and Gyroid structures, respectively. The results indicate that the FRD 30 structure experiences significantly lower stress during the initial peak. Additionally, the elastic modulus was calculated for each structure, with average values of 1392 MPa, 1765 MPa, 1745 MPa, 1457 MPa, and 1472 MPa for the FRD 30, FRD 40, FRD 45, Fischer, and Gyroid structures, respectively. The results are indicated in Figure 33.

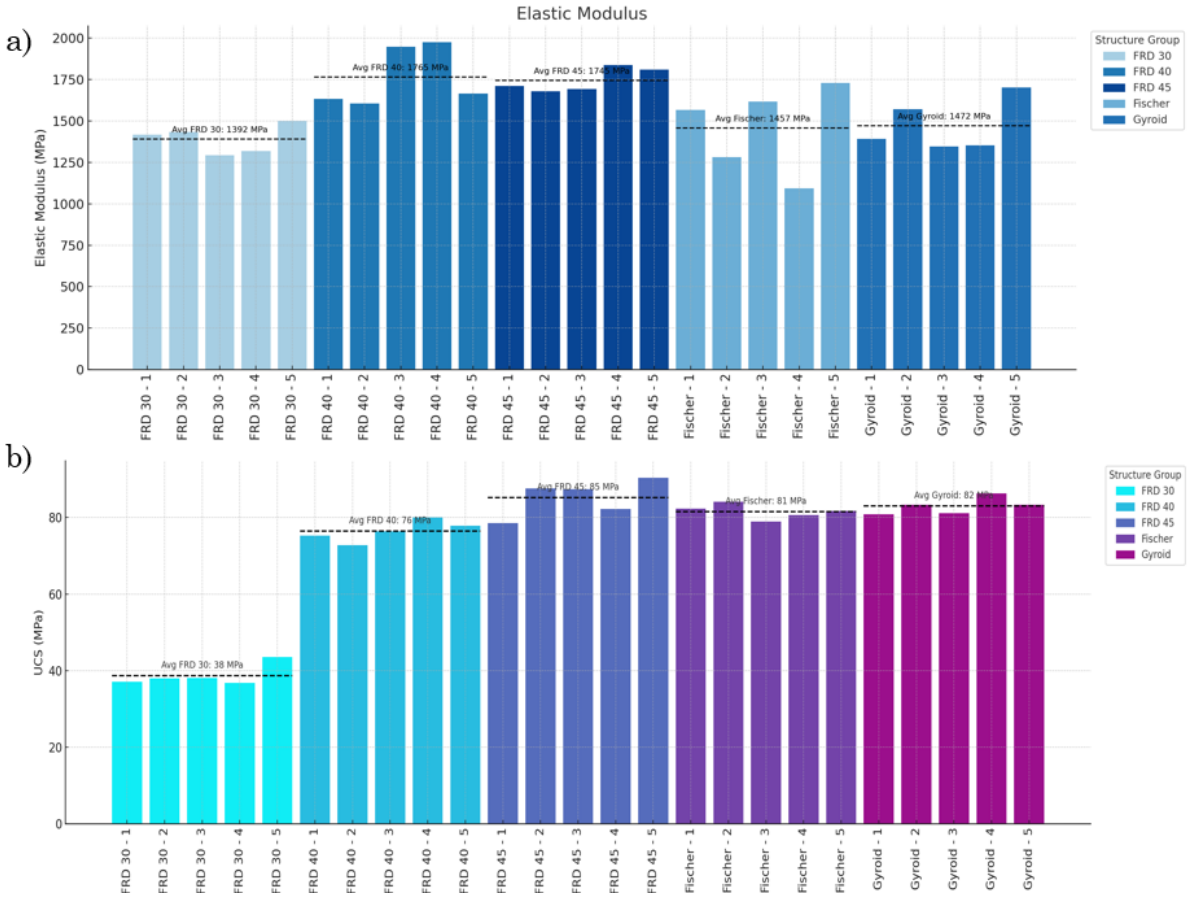

Figure 33. Elastic Modulus (a), and UCS (b) for each structure.

3.4. Ashby-Gibson Modeling

A generic relative property, which is defined as the ratio of the lattice properties to the corresponding bulk one, can be expressed as a linear relationship of the lattice relative density in a bi-logarithmic diagram, according to a model put forth by Ashby and Gibson [124] to characterize the mechanical properties of such structures. Numerous investigations [125-135] have used that model to fit the experimental mechanical properties of the structure under investigation. Every study has discovered a consistent discrepancy between the Ashby and Gibson model and the experimental findings. However, the Ashby and Gibson hypothesis states that if the relativity density is taken into account as the primary factor, an obvious pattern in the mechanical properties

should be seen. Each structure's mechanical characteristics and deviations are displayed in Figure 34 in order of relative density.

The following equation represents the relationship between Young's modulus and relative density in accordance with the Ashby and Gibson model [124]:

$$\frac{E^*}{E_s} = C_1 \left(\frac{\rho^*}{\rho_s} \right)^n \quad (3)$$

where C_1 and n are constants, E* is the cellular material's stiffness, E_s is the bulk material's stiffness, and for the bulk AlSi10Mg alloy, that value was set at 76 GPa. In a bi-logarithmic diagram, equation 3 can be shown as a straight line (the black line in Figure 34 – Left Diagram). Figure 34 also shows the experimental outcomes. similar to the Ashby and Gibson model, where the exponent of the relative density and the experimental law's constant are equal to 0.1 and 2.3 for C_1 and n, respectively. This could be explained by the fact that lattice structures are composed of cells or repeating patterns (lattice structures). In actuality, these cells' sharp edges serve as stress concentration locations, which lowers the lattice stiffness in relation to the stochastic structures (foams) that Ashby and Gibson have studied [124]. Likewise, the connection between the UCS* and the relativity density was defined by Equation 4:

$$\frac{UCS^*}{UCS_s} = C_5 \left(\frac{\rho^*}{\rho_s} \right)^m \quad (4)$$

where UCSs is the Ultimate Compressive Strength of the bulk material (which, for the AlSi10Mg alloy, is considered to be 441 MPa) and UCS* is the Ultimate Compressive Strength of the cellular material. Regarding the experimental trend, the value of the C5 and m are equal to 0.4 and 1, respectively. (Figure 34 – Right Diagram)

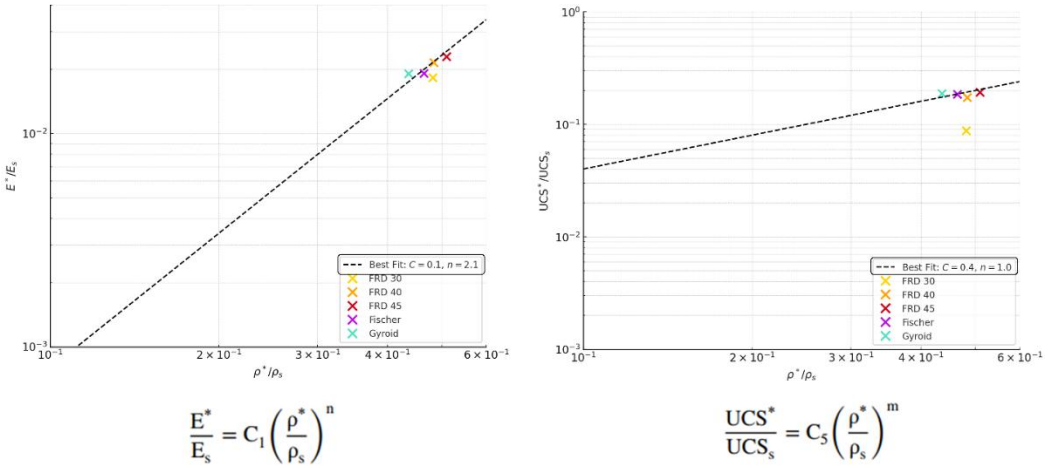

Figure 34. Ashby-Gibson modeling for Elastic modulus and UCS.

The mechanical properties of the structures have been listed in Table 7.

Table 7. Average Elastic Modulus, UCS, and Relative Densities of TPMS Structures

Structure	ρ^*/ρ_s (%)	E* (MPa)	UCS* (MPa)
FRD 30	48.15	1392.28	38.7
FRD 40	48.38	1636.93	76.46
FRD 45	50.93	1745.46	85.22
Fischer	46.42	1457.02	81.54
Gyroid	43.60	1452.02	82.96

Variations in cell type, strut length and size, and most likely surface flaws account for the variations in mechanical behavior. It should be noted that the Ashby and Gibson model does not take into account defects in the surface, which might arise from production procedures and can also be quite important. This implies that lattice structures might display a form effect based on the singular effects of the previously mentioned geometrical properties, in contrast to foams.

Numerous studies on the compressive behavior of L-PBF lattice structures compare their experimental findings with Gibson-Ashby model predictions; however, the scope of these studies restricts a more comprehensive understanding of the predictive power of the Gibson-Ashby model for L-PBF lattice structures. The obtained experimental data is contrasted with the expected range of characteristics for bending-dominated open-celled cellular structures in order to deepen this understanding (Figure 35). According to the Gibson-Ashby model, which is based on analytical modeling, extensive testing on polymeric foams, and empirical fits to experimental data, the coefficients for metallic open-celled cellular structures should fall between [0.1-4] and [0.1-1] for

modulus and strength, respectively [136]. Subsequently, based on the literature, our results fall within the mentioned range.

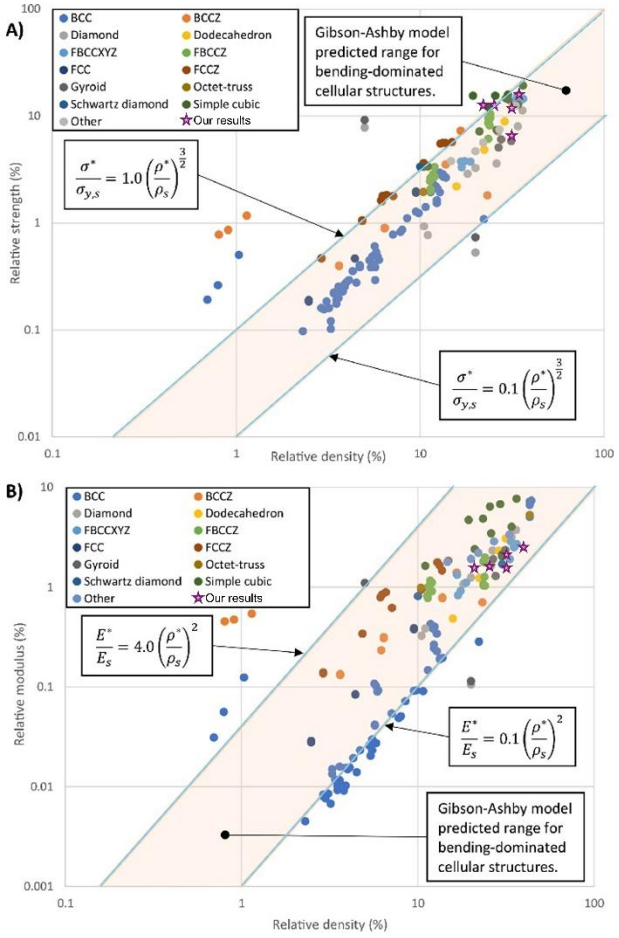

Figure 35. Gibson-Ashby model predictions are compared with reported experimental compressive strength (A) and modulus (B) data [48].

Our study's UCS and elastic modulus are higher than those reported for other lattice structures made with the same AlSi10Mg alloy (Table 8), as was previously mentioned.

Table 8. SLM lattice quasi-static compressive test data arranged by unit cell topology and collected from the literature. Ranges of reported values are represented by data. An absence of data is indicated by a dash (-).

Topology	Material	Relative density (%)	Cell size (mm)	Strut diameter (mm)	Geometry (N = nominal, M = measured)	Compressive strength (MPa)	Modulus (MPa)	Reference	Data points
BCC, BCCZ	AlSi10Mg	0.7–22.2	10	1	N, M	0.46–4.36	21.71 – 490.22	[137]	8
Octet-truss, Rhombicub octahedron	AlSi10Mg	10.4–14.7	–	–	N, M	4.7–9.1	690–1250	[138]	2

3.5. Numerical Simulation

Using the ABAQUS/Explicit solver, finite element analysis was carried out. For every model, the identical boundary conditions were used. The TPMS lattices were crushed by a rigid top plate after being positioned on a lower fixed, rigid plate [139, 140]. The top plate descended 12 mm at a steady velocity of 1 m/s, which was equivalent to 60% of the sample height. During the computation, automatic time incrementation was set, and mass scaling was not employed. Furthermore, all of the entities in the model were automatically integrated in the element-based surface and general contact method defined by ABAQUS/Explicit. The TPMS lattices had double-sided surfaces, whereas the two rigid plates had single-sided surfaces (Figure 36).

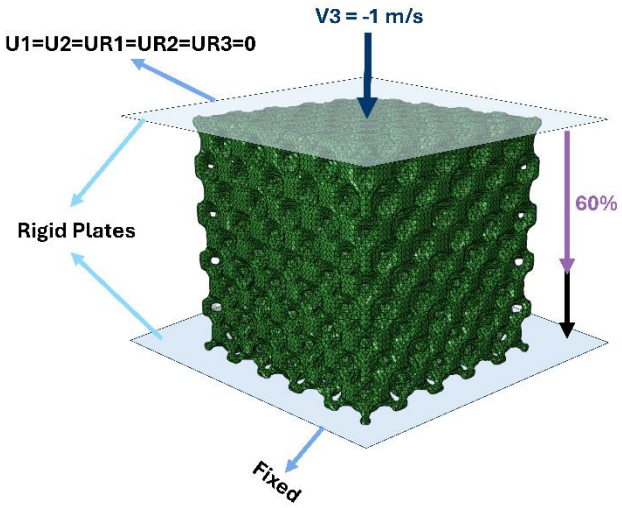

Figure 36. Boundary conditions used in the numerical study. The lower rigid plate was fully fixed in all degrees of freedom, while the upper rigid plate was loaded in the z-direction and fixed in the other five degrees of freedom. A constant velocity of 1 m/s was applied to the upper rigid plate to compress the fabricated samples up to 60% of their height.

Stress state-dependent ductile fracture is a difficult problem in computational mechanics that is required for damage modeling in order to effectively represent fracture processes [141]. Furthermore, AlSi10Mg may only undergo ductile fracture if its plastic deformation surpasses a specific threshold. Very little damage was found as a result of AlSi10Mg ductility. In earlier research, computational models could predict TPMS structures with sufficient accuracy without taking material failure or fracture into account [142, 143]. Consequently, fracture modeling was not included in this investigation.

In order to better understand the deformation behavior [144, 145]and mechanisms [146, 147], the finite element (FE) method has been widely used to numerically predict the mechanical properties of TPMS lattices, including compressive strength [148, 149] energy absorption [150], stress distribution [151], and anisotropy [152]. Choosing an appropriate element type is necessary, taking into account the computational efficiency and simulation accuracy. Regarding this, Jia et al. [153] discovered that the multi-layer models that were meshing with the shell components were

less accurate in simulating the compressive response of the P lattice structure with irregular shell thickness. For numerical simulation, a solid element model is therefore recommended. G lattice cylindrical shell (LCS) specimens discretized with four-node quadrilateral shell components with reduced integration (S4R) were investigated numerically by Wang et al. [95]. The findings showed that, with the exception of the densification stage, the computed force-displacement curve generally showed good agreement with the experimental results. Using voxelized hexahedral components for three TPMS constructions, Maskery et al. [154] discovered that the deformation mechanisms in the experiment are not adequately captured by the known FE models. Therefore, in this study we used a mesh element type of C3D4 with element size of 0.3mm in order to increase the computational efficiency based on Figure 37.

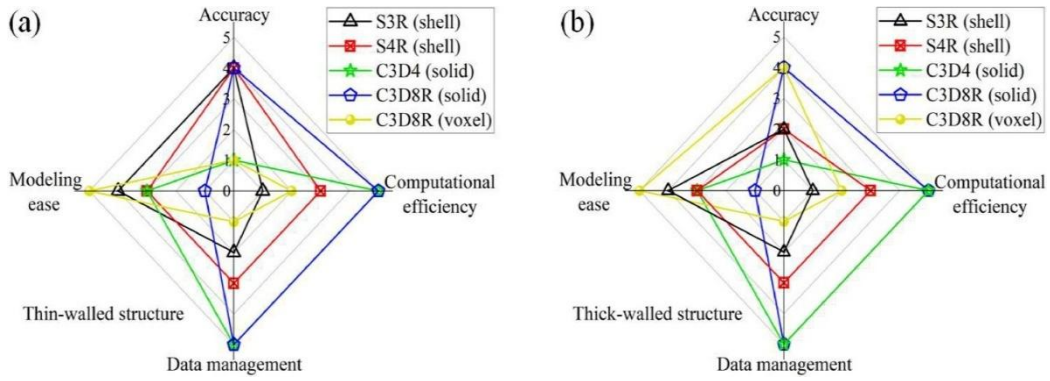

Figure 37. Comparison between different meshing strategies for (a) thin and (b) thick-walled structures (139).

Figure 38 illustrates the numerical results during quasi-static compression of the FRD–30 lattice structure, modeled using finite element simulation by ABAQUS/Explicit. The image sequence depicts von Mises stress distribution at progressive strain levels of 0%, 20%, 40%, and 60%. As the strain increases, stress localizations become more prominent, particularly near the external surfaces and contact regions of the lattice. At 0% strain, the structure remains largely undeformed, with negligible stress indicated by the dominant blue coloration. With increasing compression, the internal load-bearing elements exhibit a gradual transition from green to yellow and red, representing higher stress concentrations. By 60% strain, widespread plastic deformation is observed, with significant stress accumulation (up to +441 MPa) localized in areas subjected to buckling and collapse.

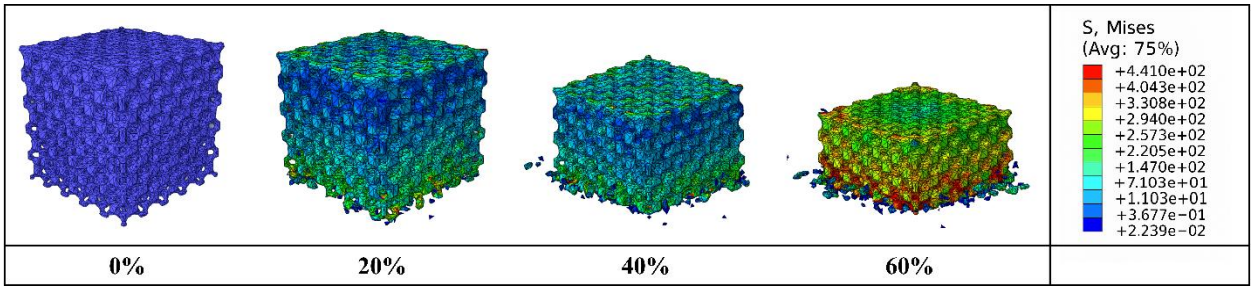

Figure 38. experimental results of quasi-static compression with finite element simulation results for FRD - 30.

Figure 39 shows the differences between the experimental results and the FE simulations. The load-displacement curves reveal that, in both plateau and densification areas, the modeling results and experimental data generally agreed well. Also, Figure 39 shows that there was a strong correlation between the experimental and numerically simulated models' deformation patterns.

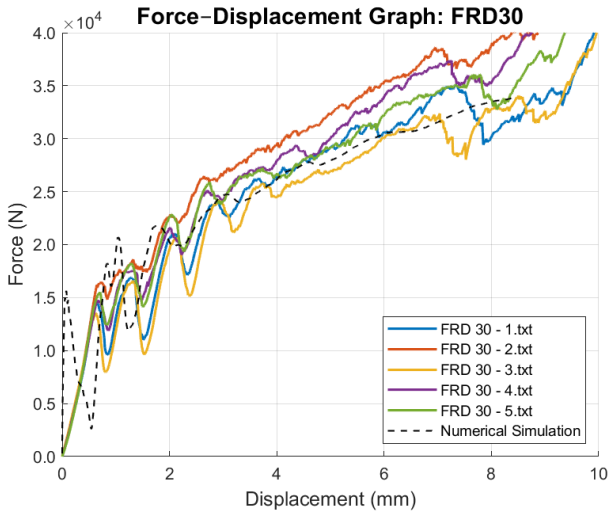

Figure 39. Load versus displacement curves for FRD - 30 TPMS structure.

3.6. Fracture Surface Analysis

One of the most popular experimental techniques for examining and analyzing solid object image characterisation of micro- and nanoparticles is the scanning electron microscope (SEM). SEM's resolution of 10 nm, is one of the reasons it is favored for particle size analysis. According to [155], more sophisticated models of these instruments can reach a resolution of roughly 2.5 nm. This tool can also be used to determine the orientation or composition of individual crystals or features in combination with other related energy-dispersive X-ray microanalysis techniques (EDX, EDS, and EDAX). Electrons are often generated using a field emission gun or tungsten filament lamps. To keep the tip free of impurities and oxide, the field emission gun needs extremely high vacuum conditions [156].

After traveling through the apertures and electromagnetic lenses, the electron beam narrows after being accelerated by the high voltage system (20 kV). After that, the beam uses scan coils to scan the specimen's surface. Following the creation of SEM-type signals from the region of beam and specimen interaction, the pictures are produced. A properly positioned detector gathers the secondary and backscattered electrons that are released from the material above the vacuum level [157](Figure 40).

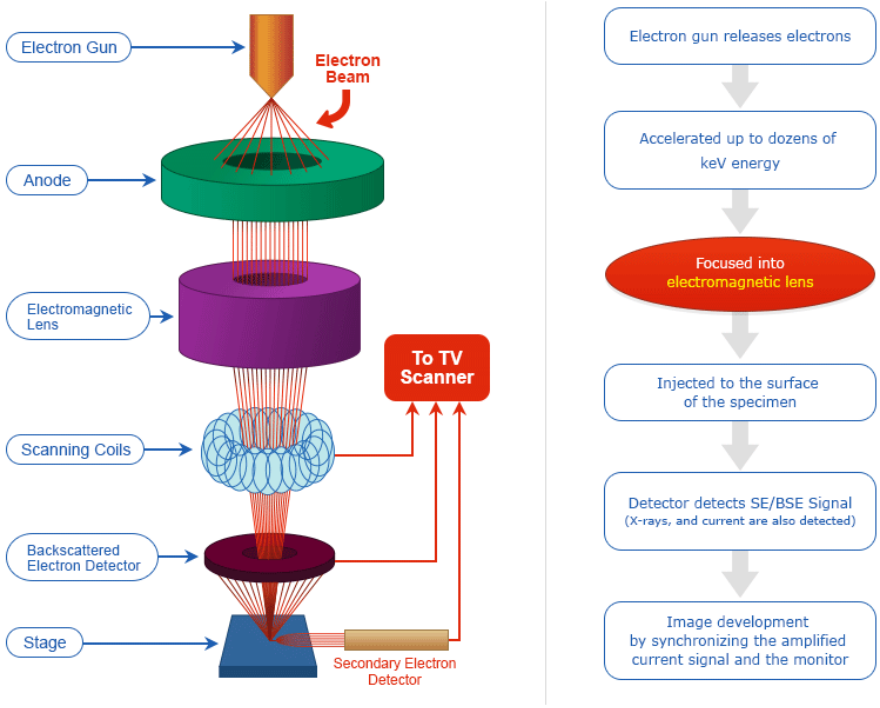

Figure 40. Schematic representation of the SEM working principle. The electron beam, generated and accelerated by the electron gun and anode, is focused by electromagnetic lenses and scanned across the sample. Signals from secondary and backscattered electrons are detected and used to construct high-resolution images.

In this study, a NeoScope JCM-6000Plus benchtop SEM (Figure 41) was employed to examine the fracture surfaces of the AM lattice structures. As illustrated in Figure 43, the SEM operates by generating a high-energy electron beam that is accelerated (up to 15 kV in this case) and focused onto the sample surface using electromagnetic lenses. The emitted secondary and backscattered electrons were detected under high-vacuum mode to obtain detailed topographical and compositional contrast. Imaging was performed at various magnifications, ranging from ×20 to ×700, to capture both general fracture morphology and localized features such as crack initiation sites, delamination zones, and unfused powder particles. This allowed for comprehensive microstructural analysis of process-induced defects and failure mechanisms. The pictures were collected from the diagonal-cut surface indicated in Figure 42.

Figure 41. JCM-6000Plus SEM used for capturing fracture morphology and localized features such as crack initation sites, delamination zones, and unfused powder particles.

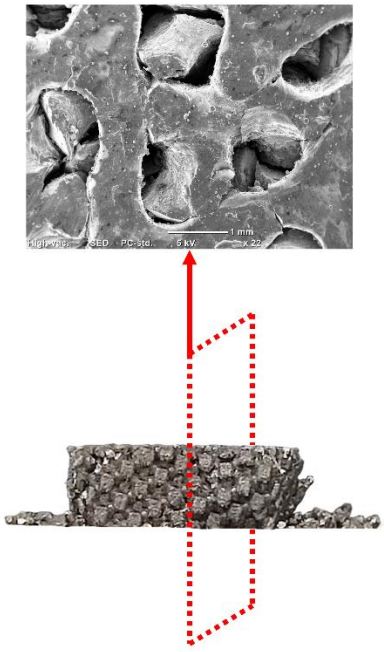

Figure 42. The plane cut used for the SEM.

The fracture surface morphology and failure processes of TPMS lattice structures made by L-PBF during quasi-static compression testing are depicted in a series of SEM pictures shown in Figure 43. Widespread intercellular cracking, with acute and uneven fractured surfaces is seen in image (a). The strut boundaries appear to be followed by the crack propagation, indicating that stress concentrations and structural discontinuities at the interconnections are crucial for the start and spread of failure.

An early-stage crack initiation zone is shown in image (b), where a microstructural defect most likely acted as a nucleation site as compressive stress increased. These imperfections are frequently linked to localized porosity or partial fusion, and they are frequently made worse by residual thermal stresses during the printing process. The lattice's mechanical integrity may be seriously affected if cracks start to form in certain areas.

A region that has experienced shear deformation is depicted in more detail in image (c), while image (c1) provides a magnified perspective of the highlighted zone. The influence of process-induced variation is reflected in the fracture surface, which shows signs of shear-induced delamination at layer boundaries. The weak interlayer adhesion inherent in layer-wise production techniques may contribute to rapid mechanical degradation, particularly under non-uniform loading, as suggested by this kind of shear failure.

The detrimental existence of unfused or partially fused powder particles trapped within the fracture surfaces is further illustrated in images (d) and (e). These particles are the result of insufficient laser exposure during the L-PBF process; they are shown by dashed red lines. They serve as local stress concentrators, increasing the formation and spread of cracks under load.

Overall, the SEM study demonstrates that shear delamination, and defect-induced cracking work together to control the failure behavior of the lattice structures. These results highlight the need for enhanced geometric design, optimum energy input, and precise process control to reduce fabrication-induced defects and improve the mechanical performance of porous materials that have been architected.

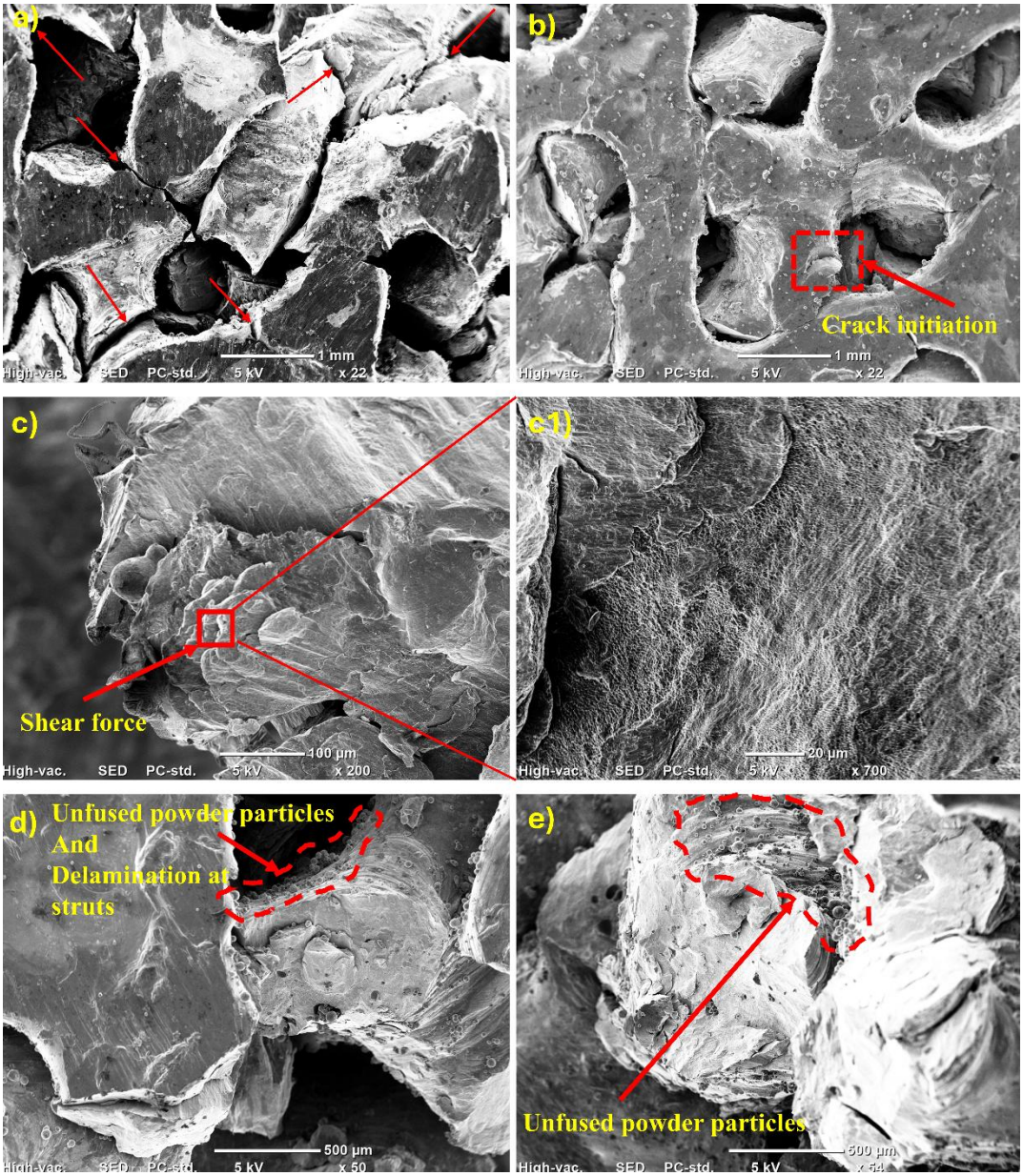

Figure 43. SEM micrographs of fracture surfaces in L-PBF-fabricated TPMS lattice structures after quasi-static compression testing. (a) Overview of intercellular brittle fracture and crack propagation along strut boundaries. (b) Evidence of crack initiation at a process-induced defect site. (c) Shear-induced delamination at strut interface; (c1) higher magnification of the boxed region showing interlayer separation. (d–e) Presence of unfused or partially fused powder particles embedded in the fracture surfaces, acting as potential crack initiation sites. These observations highlight the interplay between fabrication defects, local anisotropy, and fracture mechanisms in additively manufactured porous structures.

We investigated the fracture surfaces of two sample TPMS geometries, Gyroid (Figure 44 b–b2) and FRD-45 (Figure 44 a–a2), in order to better analyze failure processes. Progressive magnification of the FRD-45 structure (a–a2) shows a region of significant stress concentration linked to inter-layer delamination and unfused powder particles. Under mechanical loading, these manufacturing flaws act as crucial crack initiation locations and break the strut's structural continuity. The powder's spherical shape and the acute interfacial crack point to inadequate melting and inadequate layer adhesion throughout the manufacturing process. In contrast, as can be seen in the high-magnification image (b2), the Gyroid structure (b–b2) exhibits a distinct failure pattern that is dominated by internal porosities.

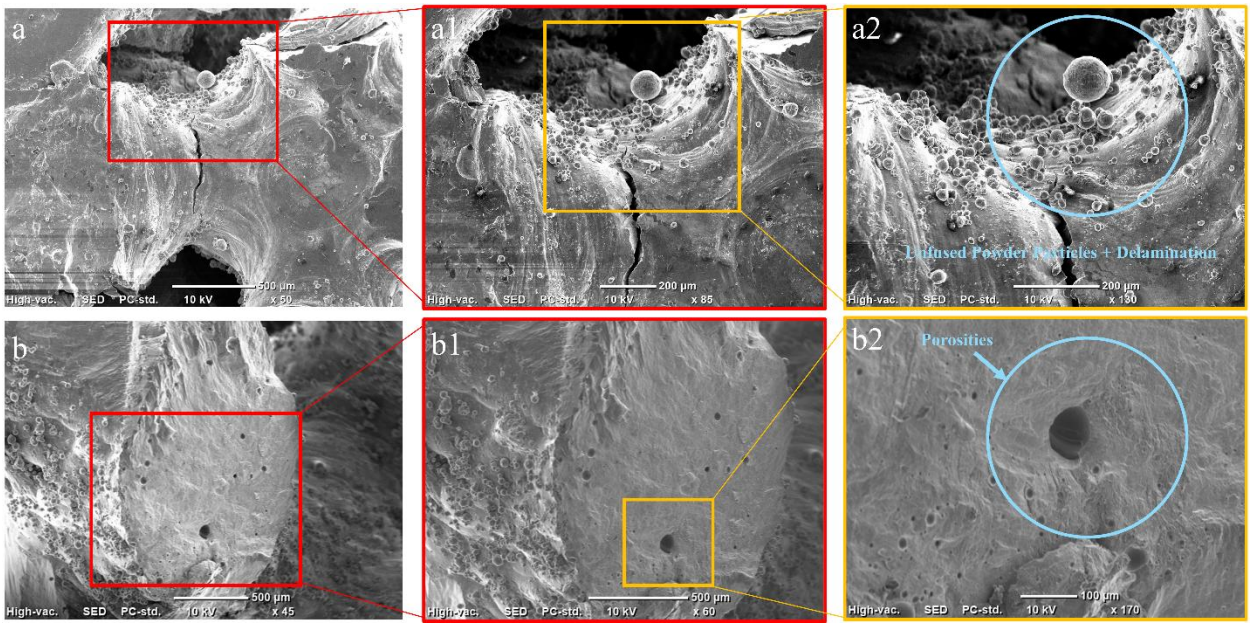

Figure 44. SEM micrographs of fracture surfaces for FRD-45 (a–a2) and Gyroid (b–b2) TPMS structures fabricated via additive manufacturing. (a–a2) illustrate unfused powder particles and delamination in the FRD-45 sample, indicating critical stress concentration regions. (b–b2) show internal porosities within the Gyroid sample, also contributing to mechanical weakening. These defects were identified as key contributors to localized failure initiation under loading.

4. Conclusion:

This thesis presented a comprehensive comparative study on the design, manufacturing, characterization, and mechanical evaluation of uniform and graded TPMS lattice structures fabricated via L-PBF. Focusing primarily on the FRD topology with comparisons to Gyroid and Fischer-Koch-S structures, the investigation aimed to elucidate how geometric grading and volume fraction distribution influence structural performance under compressive loading.

Graded lattice structures (FRD-30 and FRD-40) were successfully fabricated and compared with a uniform configuration (FRD-45), all possessing an average volume fraction of 45%. High-resolution CT analysis revealed notable differences in internal defect volume and pore morphology among structures.

Quasi-static compression experiments, performed in line with ISO 13314, revealed that graded FRD-30 structures exhibited superior deformation control and more gradual collapse behavior, relative to their uniform segments. Of all evaluated topologies, the Fischer-Koch-S lattice had the greatest specific energy absorption, validating the mechanical superiority of this design for impact-resistant applications. Among all structures, FRD-40 exhibited the highest elastic modulus, indicating superior stiffness.

Finite element simulations closely matched experimental results, confirming the predictive accuracy of the numerical model and illustrating the evolution of von Mises stress during the deformation phases. Ashby-Gibson modeling further validated that the mechanical performance of these architected materials correlates with relative density, although deviations arise from defects in manufacturing and geometry-dependent stress localization.

Furthermore, an examination of the fracture surfaces using SEM revealed important details about the TPMS structures' failure mechanisms. The pictures showed localized defects including partially fused powder particles, delamination at strut boundaries and porosities in the structures. These microstructural characteristics demonstrated the impact of manufacturing-induced defects on the deformation and failure modes by showing a strong correlation with the observed mechanical behavior. Thus, SEM improved our understanding of the progression of local damage in L-PBF-fabricated lattices by acting as a supplementary tool to XCT.

In conclusion, this work provides critical insights into the mechanical optimization of architected materials by combining experimental data, XCT-based defect analysis, SEM microstructural characterization, and validated simulations. The findings underscore the potential of grading in enhancing energy absorption, structural stability, and failure control in TPMS lattices, laying the foundation for advanced lightweight components in aerospace, automotive, mechanical and biomedical sectors.

5. References

1. Javaid, M., et al., *Role of additive manufacturing applications towards environmental sustainability.* Advanced Industrial and Engineering Polymer Research, 2021. **4**(4): p. 312-322.

2. Campbell, I., D. Bourell, and I. Gibson, *Additive manufacturing: rapid prototyping comes of age.* Rapid Prototyping Journal, 2012. **18**(4): p. 255-258.

3. Melchels, F.P.W., et al., *Additive manufacturing of tissues and organs.* Progress in Polymer Science, 2012. **37**(8): p. 1079-1104.

4. Murr, L.E., et al., *Fabrication of Metal and Alloy Components by Additive Manufacturing: Examples of 3D Materials Science.* Journal of Materials Research and Technology, 2012. **1**(1): p. 42-54.

5. Viale, V., et al., *Optimisation of downskin parameters to produce metallic parts via laser powder bed fusion process: an overview.* The International Journal of Advanced Manufacturing Technology, 2022. **123**(7): p. 2159-2182.

6. Maleki, E., et al., *Surface post-treatments for metal additive manufacturing: Progress, challenges, and opportunities.* Additive Manufacturing, 2021. **37**: p. 101619.

7. Valino, A.D., et al., *Advances in 3D printing of thermoplastic polymer composites and nanocomposites.* Progress in Polymer Science, 2019. **98**: p. 101162.

8. Stiles, A., et al., *Photopolymer formulation towards large scale additive manufacturing of autoclave capable tooling.* Additive Manufacturing, 2022. **50**: p. 102571.

9. Dadkhah, M., et al., *Additive manufacturing of ceramics: Advances, challenges, and outlook.* Journal of the European Ceramic Society, 2023. **43**(15): p. 6635-6664.

10. Wolf, A., P.L. Rosendahl, and U. Knaack, *Additive manufacturing of clay and ceramic building components.* Automation in Construction, 2022. **133**: p. 103956.

11. Taghian, M., et al., *Laser powder bed fusion of metallic components: Latest progress in productivity, quality, and cost perspectives.* Journal of Materials Research and Technology, 2023. **27**: p. 6484-6500.

12. Yuan, S., et al., *Polymeric composites for powder-based additive manufacturing: Materials and applications.* Progress in Polymer Science, 2019. **91**: p. 141-168.

13. Bose, S., et al., *Additive manufacturing of biomaterials.* Progress in Materials Science, 2018. **93**: p. 45-111.

14. Galante, R., C.G. Figueiredo-Pina, and A.P. Serro, *Additive manufacturing of ceramics for dental applications: A review.* Dental Materials, 2019. **35**(6): p. 825-846.

15. Jiang, J., et al., *A novel strategy for multi-part production in additive manufacturing.* The International Journal of Advanced Manufacturing Technology, 2020. **109**(5): p. 1237-1248.

16. Hoffmann, M. and A. Elwany, *In-Space Additive Manufacturing: A Review.* Journal of Manufacturing Science and Engineering, 2022. **145**(2).

17. Kanishka, K. and B. Acherjee, *Revolutionizing manufacturing: A comprehensive overview of additive manufacturing processes, materials, developments, and challenges.* Journal of Manufacturing Processes, 2023. **107**: p. 574-619.

18. Amaya-Rivas, J.L., et al., *Future trends of additive manufacturing in medical applications: An overview.* Heliyon, 2024. **10**(5).

19. Rahmati, S., *10.12 - Direct Rapid Tooling*, in *Comprehensive Materials Processing*, S. Hashmi, et al., Editors. 2014, Elsevier: Oxford. p. 303-344.

20. Milewski, J.O., *Additive Manufacturing of Metals: From Fundamental Technology to Rocket Nozzles, Medical Implants, and Custom Jewelry*. 2017, Cham: Springer International Publishing.

21. DebRoy, T., et al., *Additive Manufacturing of Metallic Components – Process, Structure and Properties.* Progress in Materials Science, 2018. **92**: p. 112-224.

22. Elmer, J.W., et al., *Wire-Based Additive Manufacturing of Stainless Steel Components.* Welding Journal, 2020. **99**(1): p. 8-24.

23. Panwisawas, C., Y.T. Tang, and R.C. Reed, *Metal 3D printing as a disruptive technology for superalloys.* Nature Communications, 2020. **11**(1): p. 2327.

24. Gu, D. and Y. Shen, *Balling phenomena in direct laser sintering of stainless steel powder: Metallurgical mechanisms and control methods.* Materials & Design, 2009. **30**(8): p. 2903-2910.

25. Song, Y.U., et al., *Multi-fidelity Gaussian process modeling of a thin-walled structure for laser powder bed fusion (LPBF) process window.* Journal of Manufacturing Processes, 2024. **127**: p. 107-114.

26. Abd-Elaziem, W., et al., *On the current research progress of metallic materials fabricated by laser powder bed fusion process: A review.* Journal of Materials Research and Technology, 2022. **20**: p. 681-707.

27. Frazier, W.E., *Metal additive manufacturing: a review.* Journal of Materials Engineering and Performance, 2014. **23**(6): p. 1917-1928.

28. Sames, W.J., et al., *The metallurgy and processing science of metal additive manufacturing.* International Materials Reviews, 2016. **61**(5): p. 315-360.

29. Elahinia, M., et al., *Fabrication of NiTi through additive manufacturing: a review.* Progress in Materials Science, 2016. **83**: p. 630-663.

30. Aversa, A., et al., *New Aluminum Alloys Specifically Designed for Laser Powder Bed Fusion: A Review.* Materials, 2019. **12**(7): p. 1007.

31. Zhang, B., et al., *Studies of magnetic properties of permalloy (Fe30%Ni) prepared by SLM technology.* Journal of Magnetism and Magnetic Materials, 2012. **324**: p. 495-500.

32. Fischer, M., et al., *In situ elaboration of a binary Ti-26Nb alloy by selective laser melting of elemental titanium and niobium mixed powders.* Materials Science and Engineering: C, 2016. **62**: p. 852-859.

33. Vora, P., et al., *AlSi12 in-situ alloy formation and residual stress reduction using anchorless selective laser melting.* Additive Manufacturing, 2015. **7**: p. 12-19.

34. Hu, Y. and J. Li, *Selective laser alloying of elemental titanium and boron powder: thermal models and experiment verification.* Journal of Materials Processing Technology, 2017. **249**: p. 426-432.

35. Yadroitsev, I., P. Krakhmalev, and I. Yadroitsava, *Titanium alloys manufactured by in situ alloying during laser powder bed fusion.* Journal of Materials Science, 2017. **69**: p. 2725-2730.

36. Polozov, I., et al., *Synthesis of Ti–5Al, Ti–6Al–7Nb, and Ti–22Al–25Nb alloys from elemental powders using powder-bed fusion additive manufacturing.* Journal of Alloys and Compounds, 2018. **763**: p. 436-445.

37. Simonelli, M., et al., *A comparison of Ti-6Al-4V in-situ alloying in Selective Laser Melting using simply-mixed and satellited powder blend feedstocks.* Materials Characterization, 2018: p. 0-1.

38. Biffi, C.A., et al., *Laves phases in selective laser melted TiCr1.78 alloys for hydrogen storage.* Materials Letters, 2018. **226**: p. 71-74.

39. Zhang, B., J. Chen, and C. Coddet, *Microstructure and transformation behavior of in-situ shape memory alloys by selective laser melting Ti–Ni mixed powder.* Journal of Materials Science and Technology, 2013. **29**: p. 863-867.

40. Wang, C., et al., *Additive manufacturing of NiTi shape memory alloys using pre-mixed powders.* Journal of Materials Processing Technology, 2019. **271**: p. 152-161.

41. Huang, S., et al., *Resolving the porosity-unmelted inclusion dilemma during in-situ alloying of Ti34Nb via Laser Powder Bed Fusion.* Acta Materialia, 2021. **204**: p. 116522.

42. Aboulkhair, N.T., et al., *Reducing porosity in AlSi10Mg parts processed by selective laser melting.* Additive Manufacturing, 2014. **1–4**: p. 77-86.

43. Feng, J., et al., *Triply periodic minimal surface (TPMS) porous structures: from multi-scale design, precise additive manufacturing to multidisciplinary applications.* International Journal of Extreme Manufacturing, 2022. **4**(2): p. 022001.

44. Al-Ketan, O., R. Rowshan, and R.K. Abu Al-Rub, *Topology–mechanical property relationship of 3D printed strut, skeletal, and sheet-based periodic metallic cellular materials.* Additive Manufacturing, 2018. **19**: p. 167-183.

45. Schoen, A.H., *Reflections concerning triply-periodic minimal surfaces.* Interface Focus, 2012. **2**(5): p. 658-668.

46. Yuan, L., S. Ding, and C. Wen, *Additive manufacturing technology for porous metal implant applications and triple minimal surface structures: A review.* Bioactive Materials, 2019. **4**: p. 56-70.

47. Keshavarzan, M., et al., *Investigation on the failure mechanism of triply periodic minimal surface cellular structures fabricated by vat photopolymerization additive manufacturing under compressive loadings.* Mechanics of Materials, 2020. **140**: p. 103150.

48. Maconachie, T., et al., *SLM lattice structures: Properties, performance, applications and challenges.* Materials & Design, 2019. **183**: p. 108137.

49. Riva, L., P.S. Ginestra, and E. Ceretti, *Mechanical characterization and properties of laser-based powder bed–fused lattice structures: A review.* International Journal of Advanced Manufacturing Technology, 2021. **113**: p. 649-671.

50. Yang, E., et al., *Effect of geometry on the mechanical properties of Ti-6Al-4V gyroid structures fabricated via SLM: A numerical study.* Materials & Design, 2019. **184**: p. 108165.

51. Laskowska, D., et al., *Mechanical properties and energy absorption abilities of Diamond TPMS cylindrical structures fabricated by selective laser melting with 316L stainless steel.* Materials, 2023. **16**(8): p. 3196.

52. Yin, H., et al., *Review on lattice structures for energy absorption properties.* Composite Structures, 2023. **304**: p. 116397.

53. Al-Ketan, O., et al., *Functionally graded and multi-morphology sheet TPMS lattices: Design, manufacturing, and mechanical properties.* J Mech Behav Biomed Mater, 2020. **102**: p. 103520.

54. Li, S., et al., *Functionally Graded Ti-6Al-4V Meshes with High Strength and Energy Absorption.* Advanced Engineering Materials, 2015. **18**(1): p. 34-38.

55. Maskery, I., et al., *Effective design and simulation of surface-based lattice structures featuring volume fraction and cell type grading.* Materials & Design, 2018. **155**: p. 220-232.

56. Ruiz-Cantu, L., et al., *Multi-material 3D bioprinting of porous constructs for cartilage regeneration.* Mater Sci Eng C Mater Biol Appl, 2020. **109**: p. 110578.

57. Yang, L., et al., *Continuous graded Gyroid cellular structures fabricated by selective laser melting: Design, manufacturing and mechanical properties.* Materials & Design, 2019. **162**: p. 394-404.

58. Zhang, M., et al., *Microstructure and mechanical properties of CuSn/18Ni300 bimetallic porous structures manufactured by selective laser melting.* Materials & Design, 2019. **165**.

59. Zhang, X.-Y., et al., *Effect of porosity variation strategy on the performance of functionally graded Ti-6Al-4V scaffolds for bone tissue engineering.* Materials & Design, 2018. **157**: p. 523-538.

60. Zhou, H., et al., *Sheet and network based functionally graded lattice structures manufactured by selective laser melting: Design, mechanical properties, and simulation.* International Journal of Mechanical Sciences, 2020. **175**.

61. Yang, L., et al., *Fatigue properties of Ti-6Al-4V Gyroid graded lattice structures fabricated by laser powder bed fusion with lateral loading.* Additive Manufacturing, 2021. **46**.

62. España, F.A., et al., *Design and fabrication of CoCrMo alloy based novel structures for load bearing implants using laser engineered net shaping.* Materials Science and Engineering: C, 2010. **30**(1): p. 50-57.

63. Michio Clark, J., et al., *Distribution of Brain Strain in the Cerebrum for Laboratory Impacts to Ice Hockey Goaltender Masks.* Journal of Biomechanical Engineering, 2018. **140**(12).

64. Connor, T.A., et al., *Do equestrian helmets prevent concussion? A retrospective analysis of head injuries and helmet damage from real-world equestrian accidents.* Sports Med Open, 2019. **5**(1): p. 19.

65. Maskery, I., et al., *A mechanical property evaluation of graded density Al-Si10-Mg lattice structures manufactured by selective laser melting.* Materials Science and Engineering: A, 2016. **670**: p. 264-274.

66. Maskery, I., et al., *An investigation into reinforced and functionally graded lattice structures.* Journal of Cellular Plastics, 2016. **53**(2): p. 151-165.

67. Zhang, X.Y., et al., *Topological design, permeability and mechanical behavior of additively manufactured functionally graded porous metallic biomaterials.* Acta Biomater, 2019. **84**: p. 437-452.

68. Zhang, X.-Y., et al., *Biomechanical influence of structural variation strategies on functionally graded scaffolds constructed with triply periodic minimal surface.* Additive Manufacturing, 2020. **32**.

69. Li, Y., et al., *Additively manufactured functionally graded biodegradable porous iron.* Acta Biomater, 2019. **96**: p. 646-661.

70. Yang, L., et al., *An investigation into the effect of gradients on the manufacturing fidelity of triply periodic minimal surface structures with graded density fabricated by selective laser melting.* Journal of Materials Processing Technology, 2020. **275**.

71. Caiazzo, F., V. Alfieri, and B.D. Bujazha, *Additive manufacturing of biomorphic scaffolds for bone tissue engineering.* The International Journal of Advanced Manufacturing Technology, 2021. **113**(9-10): p. 2909-2923.

72. Yin, H., et al., *Design optimization of a novel bio-inspired 3D porous structure for crashworthiness.* Composite Structures, 2021. **255 ART - 112897**.

73. de Oliveira, A.R., et al., *Compression and energy absorption of maraging steel primitive scaffolds produced by powder bed fusion.* International Journal of Advanced Manufacturing Technology, 2021. **116**: p. 1271-1283.

74. Zhao, M., et al., *Mechanical and energy absorption characteristics of additively manufactured functionally graded sheet lattice structures with minimal surfaces.* International Journal of Mechanical Sciences, 2020. **167 ART - 105262**.

75. Elmadih, W., et al., *Mechanical vibration bandgaps in surface-based lattices.* Additive Manufacturing, 2019. **25**: p. 421-429.

76. Peng, C., et al., *3D printed sandwich beams with bioinspired cores: mechanical performance and modelling.* Thin-Walled Structures, 2021. **161 ART - 107471**.

77. Alshaer, A.W. and D.J. Harland, *An investigation of the strength and stiffness of weight-saving sandwich beams with CFRP face sheets and seven 3D printed cores.* Composite Structures, 2021. **257**: p. 113391.

78. Alkebsi, E.A.A., et al., *Design of graded lattice structures in turbine blades using topology optimization.* International Journal of Computer Integrated Manufacturing, 2021. **34**(4): p. 370-384.

79. Wang, Z., et al., *Stiffness modulation for soft robot joint via lattice structure configuration design.* Procedia CIRP, 2021. **100**: p. 732-737.

80. Jiansheng Pan, A., et al., *Design and analyze of flexure hinges based on triply periodic minimal surface lattice.* Precision Engineering, 2021. **68**: p. 338-350.

81. Melchels, F.P.W., et al., *Effects of the architecture of tissue engineering scaffolds on cell seeding and culturing.* Acta Biomaterialia, 2010. **6**(11): p. 4208-4217.

82. Tikhonov, A., et al., *Stereolithographic fabrication of three-dimensional permeable scaffolds from CaP/PEGDA hydrogel biocomposites for use as bone grafts.* Journal of the Mechanical Behavior of Biomedical Materials, 2020. **110**: p. 103922.

83. Li, L., et al., *Early osteointegration evaluation of porous Ti6Al4V scaffolds designed based on triply periodic minimal surface models.* Journal of Orthopaedic Translation, 2019. **19**: p. 94-105.

84. Hsieh, M.-T., M.R. Begley, and L. Valdevit, *Architected implant designs for long bones: Advantages of minimal surface-based topologies.* Materials & Design, 2021. **207**: p. 109838.

85. Barba, D., E. Alabort, and R.C. Reed, *Synthetic bone: Design by additive manufacturing.* Acta Biomaterialia, 2019. **97**: p. 637-656.

86. Alabort, E., D. Barba, and R.C. Reed, *Design of metallic bone by additive manufacturing.* Scripta Materialia, 2019. **164**: p. 110-114.

87. Zhu, L.-y., et al., *Design and biomechanical characteristics of porous meniscal implant structures using triply periodic minimal surfaces.* Journal of Translational Medicine, 2019. **17**(1): p. 89.

88. Paré, A., et al., *Tailored Three-Dimensionally Printed Triply Periodic Calcium Phosphate Implants: A Preclinical Study for Craniofacial Bone Repair.* ACS Biomaterials Science & Engineering, 2020. **6**(1): p. 553-563.

89. Schaedler, T.A. and W.B. Carter, *Architected Cellular Materials.* Annual Review of Materials Research, 2016. **46**: p. 187-210.

90. Comi, C. and L. Driemeier, *Wave propagation in cellular locally resonant metamaterials.* Latin American Journal of Solids and Structures, 2018. **15**(4).

91. Jiang, H., et al., *Mechanical properties of 3D printed architected polymer foams under large deformation.* Materials & Design, 2020. **194**: p. 108946.

92. Abueidda, D.W., et al., *Mechanical properties of 3D printed polymeric gyroid cellular structures: experimental and finite element study.* Materials & Design, 2019. **165**: p. 107597.

93. Schoen, A.H., *Infinite periodic minimal surfaces without self-intersections*. 1970, National Aeronautics and Space Administration.

94. Maskery, I., et al., *Compressive failure modes and energy absorption in additively manufactured double gyroid lattices.* Additive Manufacturing, 2017. **16**: p. 24-29.

95. Wang, Y., et al., *Numerical and experimental studies on compressive behavior of gyroid lattice cylindrical shells.* Materials & Design, 2020. **186**: p. 108340.

96. Yan, C., et al., *Evaluations of cellular lattice structures manufactured using selective laser melting.* International Journal of Machine Tools and Manufacture, 2012. **62**: p. 32-38.

97. Yan, C., et al., *Advanced lightweight 316L stainless steel cellular lattice structures fabricated via selective laser melting.* Materials & Design, 2014. **55**: p. 533-541.

98. Li, X., L. Xiao, and W. Song, *Compressive behavior of selective laser melting printed gyroid structures under dynamic loading.* Additive Manufacturing, 2021. **46**: p. 102054.

99. Novak, N., et al., *Quasi-static and dynamic compressive behaviour of sheet TPMS cellular structures.* Composite Structures, 2021. **266**: p. 113801.

100. Abueidda, D.W., et al., *Mechanical properties of 3D printed polymeric cellular materials with triply periodic minimal surface architectures.* Materials & Design, 2017. **122**: p. 255-267.

101. Ramos, H., et al., *Response of gyroid lattice structures to impact loads.* [Journal Name Placeholder].

102. Trevisan, F., et al., *On the Selective Laser Melting (SLM) of the AlSi10Mg Alloy: Process, Microstructure, and Mechanical Properties.* Materials, 2017. **10**(1): p. 76.

103. Aversa, A., et al., *Effect of Process and Post-Process Conditions on the Mechanical Properties of an A357 Alloy Produced via Laser Powder Bed Fusion.* Metals, 2017. **7**(3): p. 68.

104. Kempen, K., et al., *Mechanical Properties of AlSi10Mg Produced by Selective Laser Melting.* Physics Procedia, 2012. **39**: p. 439-446.

105. Rao, J.H., et al., *Multiple precipitation pathways in an Al-7Si-0.6Mg alloy fabricated by selective laser melting.* Scripta Materialia, 2019. **160**: p. 66-69.

106. Olabode, M., *Weldability of High Strength Aluminium Alloys*. 2015, Lappeenranta University of Technology: Lappeenranta, Finland.

107. Tang, M., et al., *Rapid Solidification: Selective Laser Melting of AlSi10Mg.* JOM (Journal of the Minerals, Metals and Materials Society), 2016. **68**: p. 960-966.

108. Guo, H. and X. Yang, *Preparation of semi-solid slurry containing fine and globular particles for wrought aluminum alloy 2024.* Transactions of Nonferrous Metals Society of China, 2007. **17**: p. 799-804.

109. Sercombe, T.B. and X. Li, *Selective laser melting of aluminium and aluminium metal matrix composites: Review.* Materials and Manufacturing Processes, 2016. **31**: p. 77-85.

110. Boursier Niutta, C., D.S. Paolino, and A. Tridello, *Additively manufactured lattice structures: An innovative defect-based design methodology against crash impact.* Engineering Failure Analysis, 2023. **152**: p. 107436.

111. Manfredi, D., et al., *Direct Metal Laser Sintering: An additive manufacturing technology ready to produce lightweight structural parts for robotic applications.* Memorie. La Metallurgia Italiana, 2013. **10**: p. 15-24.

112. Kim, D.K., et al., *Stress partitioning behavior of an AlSi10Mg alloy produced by selective laser melting during tensile deformation using in situ neutron diffraction.* Journal of Alloys and Compounds, 2016. **686**: p. 281-286.

113. Wu, J., et al., *Microstructure and strength of selectively laser melted AlSi10Mg.* Acta Materialia, 2016. **117**: p. 311-320.

114. Mercurio, V., F. Calignano, and L. Iuliano, *Sustainable production of AlSi10Mg parts by laser powder bed fusion process.* The International Journal of Advanced Manufacturing Technology, 2023. **125**(7): p. 3117-3133.

115. Thijs, L., et al., *A study of the microstructural evolution during selective laser melting of Ti–6Al–4V.* Acta Materialia, 2010. **58**(9): p. 3303-3312.

116. Sadowski, M., et al., *Optimizing quality of additively manufactured Inconel 718 using powder bed laser melting process.* Additive Manufacturing, 2016. **11**: p. 60-70.

117. Ara, I., F. Azarmi, and X.W. Tangpong, *Microstructure Analysis of High-Density 316L Stainless Steel Manufactured by Selective Laser Melting Process.* Metallography, Microstructure, and Analysis, 2021. **10**(6): p. 754-767.

118. Ukey, K., et al., *Wire Electrical Discharge Machining (WEDM) Review on Current Optimization Research Trends.* Materials Today: Proceedings, 2023.

119. Lesko, C.C.C., L.C. Sheridan, and J.E. Gockel, *Microhardness as a Function of Process Parameters in Additively Manufactured Alloy 718.* Journal of Materials Engineering and Performance, 2021. **30**(9): p. 6630-6639.

120. Hsieh, J., *Computed Tomography: Principles, Design, Artifacts, and Recent Advances*. 2003, Bellingham, WA: SPIE Press.

121. Hsieh, J., *Computed Tomography: Principles, Design, Artifacts, and Recent Advances*. 2009, Bellingham, WA, USA: SPIE Press.

122. Roscoe, L., *Stereolithography Interface Specification*. 1988, 3D Systems Inc: Rock Hill, SC, USA.

123. Wang, D., et al., *Study on the designing rules and processability of porous structure based on selective laser melting (SLM).* Journal of Materials Processing Technology, 2013. **213**(10): p. 1734-1742.

124. Gibson, L.J. and M.F. Ashby, *Cellular Solids: Structure and Properties*. 2nd ed. 1999, Cambridge: Cambridge University Press.

125. Murr, L.E., et al., *Next-generation biomedical implants using additive manufacturing of complex, cellular and functional mesh arrays.* Philosophical Transactions of the Royal Society A Mathematical, Physical and Engineering Sciences, 2010. **368**(1917): p. 1999-2032.

126. de Formanoir, C., et al., *Improving the Mechanical Efficiency of Electron Beam Melted Titanium Lattice Structures by Chemical Etching.* Additive Manufacturing, 2016. **11**: p. 71-76.

127. Li, S.J., et al., *Compression Fatigue Behavior of Ti–6Al–4V Mesh Arrays Fabricated by Electron Beam Melting.* Acta Materialia, 2012. **60**(3): p. 793-802.

128. Cheng, X.Y., et al., *Compression deformation behavior of Ti–6Al–4V alloy with cellular structures fabricated by electron beam melting.* Journal of the Mechanical Behavior of Biomedical Materials, 2012. **16**: p. 153-162.

129. Parthasarathy, J., et al., *Mechanical evaluation of porous titanium (Ti6Al4V) structures with electron beam melting (EBM).* Journal of the Mechanical Behavior of Biomedical Materials, 2010. **3**(3): p. 249-259.

130. Cansizoglu, O., et al., *Properties of Ti–6Al–4V non-stochastic lattice structures fabricated via electron beam melting.* Materials Science and Engineering: A, 2008. **492**(1–2): p. 468-474.

131. Horn, T.J., et al., *Flexural properties of Ti6Al4V rhombic dodecahedron open cellular structures fabricated with electron beam melting.* Additive Manufacturing, 2014. **1**: p. 2-11.

132. Hernández-Nava, E., et al., *The effect of density and feature size on mechanical properties of isostructural metallic foams produced by additive manufacturing.* Acta Materialia, 2015. **85**: p. 387-395.

133. Parthasarathy, J., B. Starly, and S. Raman, *A design for the additive manufacture of functionally graded porous structures with tailored mechanical properties for biomedical applications.* Journal of Manufacturing Processes, 2011. **13**(2): p. 160-170.

134. Murr, L.E., et al., *Characterization of Ti–6Al–4V open cellular foams fabricated by additive manufacturing using electron beam melting.* Materials Science and Engineering: A, 2010. **527**(7–8): p. 1861-1868.

135. Del Guercio, G., M. Galati, and A. Saboori, *Innovative Approach to Evaluate the Mechanical Performance of Ti–6Al–4V Lattice Structures Produced by Electron Beam Melting Process.* Metals and Materials International, 2021. **27**: p. 55-67.

136. Ashby, M.F., et al., *Metal Foams: A Design Guide*. 2000: Elsevier.

137. Lei, H., et al., *Evaluation of compressive properties of SLM-fabricated multi-layer lattice structures by experimental test and μ-CT-based finite element analysis.* Materials & Design, 2019. **169**: p. 107685.

138. Arabnejad, S., et al., *High-strength porous biomaterials for bone replacement: A strategy to assess the interplay between cell morphology, mechanical properties, bone ingrowth and manufacturing constraints.* Acta Biomaterialia, 2016. **30**: p. 345-356.

139. Mozafari, A., et al., *Experimental and Numerical Crushing Analysis of a Novel Multibody Thin-Walled Circular Tube Under Axial Impact Loading.* International Journal of Applied Mechanics, 2022. **14**(09): p. 2250042.

140. Azarandaz, P., A. Mozafari, and H. Raiszade. *An Investigation on Friction Coefficients Between Multi-Body Bell-End Circular Thin-Walled Tubes*. in *2nd International Conference on Mechanics, Electrical, Aerospace Engineering and Engineering Sciences*. 2022. Iran.

141. Wu, Y., et al., *Additively Manufactured Materials and Structures: A State-of-the-Art Review on Their Mechanical Characteristics and Energy Absorption.* International Journal of Mechanical Sciences, 2023. **246**: p. 108102.

142. Zhang, L., et al., *Energy Absorption Characteristics of Metallic Triply Periodic Minimal Surface Sheet Structures Under Compressive Loading.* Additive Manufacturing, 2018. **23**: p. 505-515.

143. Chan, K.S., et al., *Fatigue Life of Titanium Alloys Fabricated by Additive Layer Manufacturing Techniques for Dental Implants.* Metallurgical and Materials Transactions A, 2013. **44**(2): p. 1010-1022.

144. Cansizoglu, O., et al., *Properties of Ti–6Al–4V Non-Stochastic Lattice Structures Fabricated via Electron Beam Melting.* Materials Science and Engineering: A, 2008. **492**(1-2): p. 468-474.

145. Zhang, B., et al., *Energy Absorption Behaviors and Optimization Design of Thin-Walled Double-Hat Beam Under Bending.* Thin-Walled Structures, 2022. **179**: p. 109577.

146. Shi, X., et al., *Comparison of Compression Performance and Energy Absorption of Lattice Structures Fabricated by Selective Laser Melting.* Advanced Engineering Materials, 2020. **22**(11): p. 2000453.

147. Xu, X., et al., *Axial Mechanical Properties and Robust Optimization of Foam-Filled Hierarchical Structures.* Composite Structures, 2022. **289**: p. 115501.

148. Afshar, M., A. Pourkamali Anaraki, and H. Montazerian, *Compressive Characteristics of Radially Graded Porosity Scaffolds Architectured with Minimal Surfaces.* Materials Science and Engineering: C, 2018. **92**: p. 254-267.

149. Wang, Y., et al., *Cell-Size Graded Sandwich Enhances Additive Manufacturing Fidelity and Energy Absorption.* International Journal of Mechanical Sciences, 2021. **211**: p. 106798.

150. Kladovasilakis, N., K. Tsongas, and D. Tzetzis, *Mechanical and FEA-Assisted Characterization of Fused Filament Fabricated Triply Periodic Minimal Surface Structures.* Journal of Composites Science, 2021. **5**(2): p. 58.

151. Ren, F., et al., *Transition Boundaries and Stiffness Optimal Design for Multi-TPMS Lattices.* Materials & Design, 2021. **210**: p. 110062.

152. Li, D., et al., *Comparison of Mechanical Properties and Energy Absorption of Sheet-Based and Strut-Based Gyroid Cellular Structures with Graded Densities.* Materials, 2019. **12**(13): p. 2183.

153. Jia, H., et al., *An Experimental and Numerical Investigation of Compressive Response of Designed Schwarz Primitive Triply Periodic Minimal Surface with Non-Uniform Shell Thickness.* Extreme Mechanics Letters, 2020. **37**: p. 100671.

154. Maskery, I., et al., *Insights into the Mechanical Properties of Several Triply Periodic Minimal Surface Lattice Structures Made by Polymer Additive Manufacturing.* Polymer, 2017. **152**: p. 62-71.

155. Goldstein, J.I., et al., *Scanning electron microscopy and X-ray microanalysis*. 2017: springer.

156. Pathak, Y. and D. Thassu, *Drug delivery nanoparticles formulation and characterization.* Drugs and the pharmaceutical sciences, 2009. **191**: p. 16-34.

157. Hafner, B., *Scanning electron microscopy primer.* Characterization Facility, University of Minnesota-Twin Cities, 2007: p. 1-29.